

Quantitative determination of optical and recombination losses in thin-film photovoltaic devices based on external quantum efficiency analysis

Akihiro Nakane,¹ Hitoshi Tampo,² Masato Tamakoshi,¹ Shohei Fujimoto,¹ Kang Min Kim,² Shinho Kim,² Hajime Shibata,² Shigeru Niki,² and Hiroyuki Fujiwara^{1,a)}

¹Department of Electrical, Electronic and Computer Engineering, Gifu University, 1-1 Yanagido, Gifu 501-1193, Japan

²Research Center for Photovoltaics, National Institute of Advanced Industrial Science and Technology (AIST), Central2, 1-1-1 Umezono, Tsukuba, Ibaraki 305-8568, Japan

Abstract

In developing photovoltaic devices with high efficiencies, quantitative determination of the carrier loss is crucial. In conventional solar-cell characterization techniques, however, photocurrent reduction originating from parasitic light absorption and carrier recombination within the light absorber cannot be assessed easily. Here, we develop a general analysis scheme in which the optical and recombination losses in submicron-textured solar cells are evaluated systematically from external quantum efficiency (EQE) spectra. In this method, the optical absorption in solar cells is first deduced by imposing the anti-reflection condition in the calculation of the absorptance spectrum, and the carrier extraction from the light absorber layer is then modeled by considering a carrier collection length from the absorber interface. Our analysis method is appropriate for a wide variety of photovoltaic devices, including kesterite solar cells [$\text{Cu}_2\text{ZnSnSe}_4$, $\text{Cu}_2\text{ZnSnS}_4$, and $\text{Cu}_2\text{ZnSn}(\text{S},\text{Se})_4$], zincblende CdTe solar cells, and hybrid perovskite ($\text{CH}_3\text{NH}_3\text{PbI}_3$) solar cells, and provides excellent fitting to numerous EQE spectra reported earlier. Based on the results obtained from our EQE analyses, we discuss the effects of parasitic absorption and carrier recombination in different types of solar cells.

^{a)}Author to whom correspondence should be addressed. Electronic mail: fujiwara@gifu-u.ac.jp.

I. INTRODUCTION

Conversion efficiency of solar cells is influenced by a variety of physical and optical properties of constituent layers and, in solar cell optimization, it is necessary to identify and improve the limiting factors. In photovoltaic devices, the extraction of photo-generated carriers from a semiconductor light absorber is an essential process and the presence of recombination centers within absorber layers deteriorates the short-circuit current density (J_{sc}) significantly.¹ The effect of the recombination generally becomes more severe in the solar-cell bottom region, where the generated carriers need to reach the front interface through carrier diffusion. In other words, solar cell efficiencies are often limited by the diffusion length (L_D) of photo-generated carriers.¹

Unfortunately, the evaluation of L_D in thin-film solar cells has been rather challenging. Although the L_D of solar cells can be evaluated from electron-beam induced current (EBIC)²⁻⁵ and photoluminescence (PL) lifetime⁶⁻⁸ measurements, the interpretation of the EBIC and PL data is not straight forward. Specifically, in the EBIC characterization of thin-film solar cells, the electron beam size is often comparable to the absorber thickness, and the EBIC signal may change by the effects of surface recombination and injection density.⁹ The PL signals are also influenced by multiple factors, including bulk life time, interface recombination, carrier mobility, and injection/doping density.¹⁰ Moreover, for CuInGaSe₂ (CIGSe) solar cells, the PL lifetime decreases by two orders of magnitude after the CIGSe surface is exposed to air for 1 day and the strong laser-light illumination induces the degradation.¹¹

One alternative method that can be used for the accurate L_D evaluation is the quantum efficiency (QE) analysis.¹²⁻¹⁸ Since the QE spectra contain the depth information due to the wavelength (λ)-dependent penetration depth of light, the L_D can be deduced from the QE response in the long λ region near the band gap (E_g).¹⁵⁻¹⁸ By analyzing the QE spectra obtained at different bias voltages, the recombination mechanism can further be studied.¹⁸ In the conventional QE characterization, however, the QE spectra are analyzed without considering optical effects induced by light scattering and parasitic light absorption in the transparent conductive oxide (TCO) and metal back electrode. Thus, the optical losses within solar cell devices are not generally clear.

In our previous study, on the other hand, we have developed an external QE (EQE) simulation method that can be applied to the explicit optical simulation of submicron-textured CIGSe solar cells.¹⁹ Although the EQE simulation generally becomes difficult when textured structures are present,²⁰⁻²² our method allows the

accurate determination of the EQE spectra without considering three-dimensional structures. This method is based on the finding that the optical effect of submicron rough textures is mainly the elimination of interference pattern.¹⁹ In the simulation of this method, the optical response of the light absorber is estimated by simply forcing the anti-reflection condition in a perfectly flat optical system. From this simple optical simulation method using the anti-reflection condition (hereafter denoted as ARC method), the EQE spectrum of CIGSe solar cells fabricated by a standard three-stage evaporation process has been reproduced almost perfectly.¹⁹

Quite fortunately, the ARC method is a general method and can be applied to other thin-film photovoltaic devices without any restrictions. Since accurate optical simulation for arbitrary thin film structures can now be performed based on the ARC method, if the carrier extraction or recombination is further assumed in this simulation, both optical and recombination losses can be evaluated simultaneously from conventional EQE spectra. Such EQE analyses can be employed systematically to fill the strong need for revealing limiting physical/optical factors in solar cell devices.

In this study, we have established a general EQE analysis method in which the effect of the carrier recombination in the light absorber layer is further modeled within the framework of the ARC method. In this extended ARC method (hereafter denoted as e-ARC method), the carrier extraction from the light absorber is expressed by a simple exponential decaying function. Although the determination of L_D is preferred, we have focused on the quantitative analysis of the recombination loss, and we have greatly simplified the QE analysis by considering only the effective carrier-collection length from the absorber front interface. Even though the recombination mechanism cannot be characterized from our EQE analysis, the developed e-ARC method is quite effective in determining the recombination loss that occurs in solar-cell bottom region. We demonstrate that the e-ARC method can be employed to deduce J_{sc} losses induced by parasitic optical absorption and carrier recombination in a variety of solar cell devices including $\text{Cu}_2\text{ZnSnSe}_4$ (CZTSe),^{16,23-30} $\text{Cu}_2\text{ZnSnS}_4$ (CZTS),³¹⁻³⁹ CZTSSe,^{17,40-47} CdTe,⁴⁸ and $\text{CH}_3\text{NH}_3\text{PbI}_3$ hybrid perovskite^{49,50} solar cells.

II. EXPERIMENT

For the EQE analysis of a CZTSe solar cell, we fabricated a device consisting of (Al grid)/ZnO:Al/non-doped ZnO/CdS/CZTSe/Mo/soda lime glass substrate.⁵¹ The CZTSe layer in the solar cell was prepared by a single coevaporation process of Cu, Zn, Sn and Se elementary sources at 340 °C, followed by thermal annealing at 550 °C under Se and

SnSe₂ atmosphere. We determined the composition of the CZTSe layer from electron probe microanalyzer (Cu:Zn:Sn:Se = 1.80:1.31:0.89:4.00) and, for this layer, the compositional ratios of Cu/(Zn+Sn) = 0.82 and Zn/Sn = 1.47 were estimated. In the fabrication of the CZTSe solar cell, the CdS layer was formed on the CZTSe layer by a standard chemical-bath deposition technique,⁵² whereas we fabricated the non-doped ZnO, ZnO:Al and Mo layers by sputtering.

Figure 1 shows the cross-sectional transmission electron microscopy (TEM) images of the CZTSe solar cell fabricated in this study: (a) the whole solar-cell structure, (b) the enlarged image for the ZnO/CdS/CZTSe interface, and (c) the enlarged image for the CZTSe/Mo interface. When the CZTSe layer is prepared by the single coevaporation, the void-rich interface structure is formed on the substrate. Similar non-uniform interface structures have been observed in other CZTSe solar cells.^{28,30,53} The CZTSe solar-cell structure similar to Fig. 1(a) has also been confirmed in the corresponding scanning electron microscope (SEM) images. However, the void structure at the interface is more pronounced in the TEM images, as the focused-ion-beam process, used in the TEM sample preparation, tends to increase the interface void fraction.

In the TEM image of Fig. 1(b), the polycrystalline CdS layer covers the CZTSe layer uniformly with a thickness of 70 nm. Moreover, a uniform layer with a thickness of 150 nm is present between the CZTSe and Mo layers [Fig. 1(c)]. From the compositional analysis of this layer, we confirmed that this layer is MoSe₂, in agreement with earlier CZT(S)Se studies.^{17,25,53-55} In the initial deposition process, therefore, the MoSe₂ layer is first formed on the Mo substrate by the excessive Se supply,⁵⁵ followed by the CZTSe formation on the MoSe₂ layer. The generation of the void-rich structure at the interface could be related to the poor adhesion of the CZTSe to the MoSe₂ layer. It should be noted that the thickness of the MoSe₂ layer formed during the CZTSe growth is much thicker than that formed during the CIGSe growth.¹⁹

For the CZTSe solar cell of Fig. 1, we obtained a conversion efficiency of 8.46% with a J_{sc} of 33.4 mA/cm², an open-circuit voltage (V_{oc}) of 418 mV and a fill factor (FF) of 0.606. In the EQE measurement of this solar cell, however, we obtained a slightly smaller J_{sc} value of 31.6 mA/cm² in part due to the difference in the light illumination conditions between the current-voltage and EQE measurements. Specifically, in the EQE measurement, the effect of the carrier recombination is expected to become more significant since the photocurrent generated at a selected λ is much weaker than that under AM1.5G illumination. In this study, we have analyzed the EQE spectrum obtained from the CZTSe solar cell in Fig. 1 to establish a general EQE analysis procedure.

III. EQE ANALYSIS

A. Calculation method

The EQE spectra of all solar cells, including CZTSe, CZTS, CZTSSe, CdTe and $\text{CH}_3\text{NH}_3\text{PbI}_3$ solar cells, were calculated based on the e-ARC method established in this study. In this method, the optical response of solar cell structures is calculated first from the conventional optical-admittance method⁵⁶⁻⁵⁸ assuming a perfectly flat device structure. Figure 2(a) indicates the calculation procedure of this optical admittance method. In this figure, N_j shows the complex refractive index ($N_j = n_j - ik_j$) defined from the refractive index n and the extinction coefficient k , whereas Y_j , ψ_j , and d_j denote the optical admittance, potential transmittance, and thickness of the j th layer, respectively. In this optical model, $j = 0$ corresponds to the ambient environment (air).

Using the magnetic field (H_f) and electric field (E_f), the optical admittance is expressed as $Y = H_f/E_f$. For non-absorbing media ($k = 0$), there is a general relation of $H_f = nE_f$ and the same relation holds for N ($H_f = NE_f$). Thus, Y basically represents N , and Y of the substrate is expressed as $Y_j = N_{j+1}$. From a matrix calculation that satisfies the boundary conditions of (E_f , H_f), Y_j at the interface of N_j/N_{j+1} can be transferred to Y_{j-1} by

$$Y_{j-1} = \frac{Y_j \cos \delta_j + iN_j \sin \delta_j}{\cos \delta_j + iY_j \sin \delta_j / N_j}. \quad (1)$$

Here, δ_j denotes the phase thickness expressed by $\delta_j = 2\pi N_j d_j / \lambda$. If the similar calculation is repeated in a multilayer stack, we finally obtain Y_0 , from which the reflectance of the flat structure (R_{flat}) is calculated as

$$R_{\text{flat}} = |1 - Y_0|^2 / |1 + Y_0|^2. \quad (2)$$

From Eqs. (1) and (2), therefore, R_{flat} can be obtained relatively easily if N_j and d_j of all the optical layers are known.

In the optical admittance method, the light absorption in each layer is determined by considering the light transmittance (T) at each interface. If the light intensity is $I = 1$, T at the top surface is expressed by $T = 1 - R_{\text{flat}}$. The T value at the interface of the second or higher layer can then be calculated by multiplying ψ of each layer sequentially from the top layer, as shown in Fig. 2(a), and ψ_j is given by

$$\psi_j = \frac{\text{Re}(Y_j)}{\text{Re}(Y_{j-1}) \left| \cos \delta_j + iY_j \sin \delta_j / N_j \right|^2}. \quad (3)$$

From R_{flat} and ψ of each layer, the absorptance in the j th layer (A_j) is expressed by

$$A_j = (1 - R_{\text{flat}})(1 - \psi_j) \prod_{k=1}^{j-1} \psi_k. \quad (4)$$

Based on the above procedure, the absorptance in each solar-cell component layer is determined from the top to bottom layer ($A_1 \rightarrow A_j$).

Figure 2(b) shows the optical model constructed for the CZTSe solar cell in Fig. 1. In this model, the layer thicknesses deduced from the TEM measurements in Fig. 1 are shown. However, the thickness of the non-doped ZnO layer cannot be distinguished in the TEM image and was determined from a thickness of a single ZnO layer formed separately on a different substrate (50 nm). The optical effect of the void-rich rear interface structure was expressed by assuming a void volume fraction of 30 vol.% in the CZTSe bottom layer with a thickness of 310 nm. To calculate the optical properties of this bottom layer, we employed the Bruggeman effective-medium approximation.^{59,60} From the EQE simulations, we confirmed that the void volume fraction in the bottom region does not affect the EQE spectrum of the CZTSe solar cell significantly.

Figure 3 summarizes the calculation procedure of the e-ARC method. This EQE simulation was performed by the optical model of Fig. 2(b) using reported optical constants of CZTSe,⁶¹ ZnO:Al,¹⁹ non-doped ZnO,¹⁹ CdS,^{19,62} MoSe₂,^{19,63} and Mo.¹⁹ In Fig. 3(a), R_{flat} of the CZTSe solar cell, calculated from Eqs. (1) and (2), is shown. When the flat layer structure is assumed, the absolute value of R_{flat} varies largely versus λ by the optical interference effect. In Fig. 3(a), A_{flat} represents the A spectrum of the CZTSe layer obtained from R_{flat} using Eq. (4). In this case, A_{flat} is modulated strongly by the large optical interference, and the absolute values of A_{flat} reduce in the λ region where R_{flat} is large. It should be emphasized that the A_{flat} spectrum obtained assuming the flat structure is quite different from the EQE spectra reported for CZTSe solar cells.^{16,23-30} The large discrepancy can be attributed to the presence of natural textures (see Fig. 1), which induces relatively large light scattering.

In our previous study for CIGSe solar cells, we found that the optical effect of the submicron texture is mainly the elimination of the optical interference pattern and can be approximated by linearly connecting the minimum positions that appear in R_{flat} .¹⁹ In Fig. 3(a), R_{tex} represents the reflectance spectrum obtained from this procedure and the minimum R_{flat} positions are denoted by the red circles. By simply connecting these red circles, the R spectrum for a submicron-textured structure (R_{tex}) can be deduced without any knowledge of geometrical structures. The A spectrum corresponding to the textured structure (A_{tex}) can then be obtained easily by replacing R_{flat} in Eq. (4) with R_{tex} . In the optical model of Fig. 2(b), however, there is the CZTSe/void layer, in addition to the

uniform CZTSe layer. For this structure, A_{flat} and A_{tex} in Fig. 3(a) have been obtained by simply adding the corresponding A spectra obtained from these two layers.

In a multilayer system, the minimum positions in the R_{flat} spectrum basically satisfy the anti-reflection condition, in which the multiply reflected beams generated within a layered structure are out of phase. In the established method, the anti-reflection condition is superimposed on the result of R_{flat} to express the interference-fringe elimination by natural textures. It can be seen from Fig. 3(a) that the yellow area, which corresponds to the difference between A_{flat} and A_{tex} , is absorbed additionally by assuming the anti-reflection condition. From the above approach (ARC method), the EQE spectra of CIGSe solar cells are reproduced almost perfectly.¹⁹ The calculation of textured solar cells can be performed more easily by using experimental R spectra obtained from actual solar cell structures. In this case, the experimental R spectrum is used directly in the calculation of Eq. (4), instead of R_{tex} .¹⁹

In this study, by further modeling the carrier collection within the light absorber layer, we have developed the e-ARC method. To simplify the analysis, we describe the carrier collection efficiency (H) by considering the carrier collection length (L_C) from the absorber interface as follows:

$$H_1(\lambda) = 1 - \exp[-\alpha(\lambda)L_C]. \quad (5)$$

Here, $H_1(\lambda)$ denotes the carrier collection model expressed by Eq. (5) and the α shows the absorption coefficient of absorber layers. This model is equivalent to the light absorption expressed by the Beer's law, $A(\lambda) = 1 - \exp[-\alpha(\lambda)d]$, where d shows the distance from the surface (or interface).⁵⁹ The $H_1(\lambda)$ obtained from Eq. (5) represents the light absorption at depth L_C from the surface of materials having infinite thickness. In this model, therefore, the optical confinement effect, induced by the back-side reflection and the resulting multiple light reflection within the absorber layer, is neglected completely. Using Eq. (5), the simple optical simulation of internal QE (IQE) was also performed,^{1,64} but such efforts have been limited. In Eq. (5), L_C can be considered as an effective length where minority carriers in the absorber layer are extracted efficiently and the relation between L_C and L_D is expressed as

$$L_C = L_D + W, \quad (6)$$

where W indicates the depletion layer thickness.¹ In the model of $H_1(\lambda)$, the influences of the carrier diffusion and carrier drift in the space-charge region are not described separately. Moreover, the effects of the band offset and the carrier recombinations that occur in the bulk, interface (front or rear) and grain-boundary regions are not specifically modeled. The significance of the $H_1(\lambda)$ model is that all the complex effects concerning the carrier collection are represented by a single analysis parameter of L_C .

Figure 3(b) shows $H_1(\lambda)$ calculated from $\alpha(\lambda)$ of the CZTSe using Eq. (5). When L_C is infinite ($L_C = \infty$), we obtain $H_1(\lambda) = 1$ in the energy region above the absorption edge of the CZTSe [$\lambda \leq 1770$ nm in Fig. 3(b)]. As L_C decreases, the H_1 value in the longer λ region gradually reduces. In the calculation of $H_1(\lambda)$ using Eq. (5), however, it is necessary to use unrealistic L_C values that are far larger than the total thickness of the absorber layer (~ 1 μm in Fig. 1). In particular, to obtain the sufficiently high $H_1(\lambda)$ values in the low α region, quite high L_C values need to be used. Moreover, when the optical confinement is strong, L_C values obtained by applying Eq. (5) also increase, as the effective optical-pass length increases in this case. Thus, L_C defined by Eq. (5) should be considered as a parameter (reference) value. However, when L_C is smaller than the absorber layer thickness, L_C approximates a real physical value.

Although $H_1(\lambda)$ in Eq. (5) is a rather practical model, a more exact equation for $H(\lambda)$ has been derived by solving the carrier continuity equation:^{12,13}

$$H_2(\lambda) = 1 - \exp[-\alpha(\lambda)W]/[1 + \alpha(\lambda)L_D]. \quad (7)$$

In this study, the carrier collection model expressed by Eq. (7) is denoted as $H_2(\lambda)$. If this model is applied for the EQE analysis, the parameters (W , L_D) can be deduced from the fitting analysis of the EQE spectrum. Nevertheless, Eq. (7) has also been derived by neglecting the optical interference effect in absorber layers. So far, using $H_2(\lambda)$, simple QE analyses have been made assuming $H_2(\lambda) = IQE(\lambda)$ [or $EQE(\lambda)$].¹⁵⁻¹⁷ It should be noted that, if $L_D = 0$ is assumed in the models of $H_1(\lambda)$ and $H_2(\lambda)$ [i.e., $L_C = W$ in Eqs. (5) and (6)], both models are reduced to the same form of $H(\lambda) = 1 - \exp[-\alpha(\lambda)W]$. In the model of $H_1(\lambda)$, however, the carrier collection by the carrier drift and diffusion is approximated by using a single parameter of L_C and the relation of $L_C = W$ is not always valid.

In this study, the EQE analyses are performed by employing both $H_1(\lambda)$ and $H_2(\lambda)$. However, the analysis and interpretation of the data are simplified greatly when $H_1(\lambda)$ is used. Thus, we implemented the EQE analyses of various solar cells by using $H_1(\lambda)$, unless otherwise stated. The EQE analysis using $H_1(\lambda)$ is also advantageous when the two parameters (W , L_D) in $H_2(\lambda)$ show high correlation in the EQE fitting analysis.

In the e-ARC method, the EQE spectrum is estimated quite simply as

$$EQE(\lambda) = A_{\text{tex}}(\lambda)H(\lambda). \quad (8)$$

Figure 3(c) shows the EQE spectra calculated from the e-ARC method using A_{tex} in Fig. 3(a) and $H_1(\lambda)$ in Fig. 3(b). In the case of $L_C = \infty$ [or $H_1(\lambda) = 1$], we obtain $EQE(\lambda) = A_{\text{tex}}(\lambda)$. This EQE spectrum corresponds to the one calculated from the ARC method, in which no carrier recombination is assumed to occur. In the EQE spectra calculated from the e-ARC method, however, the EQE response in the longer λ region decreases as the

L_C value reduces due to the limited carrier extraction. From the EQE spectrum calculated using the e-ARC method, the recombination loss can be estimated further as a difference from a baseline EQE spectrum of $L_C = \infty$. In the developed method, therefore, the recombination loss is calculated quantitatively using L_C as a sole parameter. It should be noted that, when the total thickness of the light absorber is modified, the optical interference and back-side reflection in solar cells change significantly.⁶⁵ Thus, it is necessary to model the carrier generation and collection separately.

From the EQE spectrum deduced by Eq. (8), J_{sc} of the solar cell is finally calculated as

$$J_{sc} = \frac{e\lambda}{2\pi\hbar c} \int EQE(\lambda)F(\lambda)d\lambda, \quad (9)$$

where e and c are the electron charge and the speed of light, respectively. In Eq. (9), $F(\lambda)$ indicates the solar irradiance in units of $\text{W cm}^{-2} \text{nm}^{-1}$ under AM1.5G illumination.

B. Dielectric function

Figure 4 summarizes (a) the ε_2 spectra of the dielectric functions ($\varepsilon = \varepsilon_1 - i\varepsilon_2 = N^2$) and (b) the α spectra of Cu_2SnSe_3 (CTSe), CZTSe, CuInSe_2 (CISE), CZTS, CuGaSe_2 (CGSe), CdTe and $\text{CH}_3\text{NH}_3\text{PbI}_3$ absorber layers used for the EQE analyses and simulations. These dielectric functions are the reported data of CTSe,⁶¹ CZTSe,⁶¹ CISE,^{66,67} CZTS,⁶⁸ CGSe,^{66,67} CdTe,⁶⁹ and $\text{CH}_3\text{NH}_3\text{PbI}_3$.⁶⁵ The onset of the light absorption ($\varepsilon_2 > 0$) basically corresponds to E_g and, for the Cu-Se semiconductors, the E_g values are 0.68 eV (CTSe),⁶¹ 0.91 eV (CZTSe),⁶¹ 1.00 eV (CISE),⁶⁶ 1.32 eV (CZTS),⁶⁸ and 1.70 eV (CGSe).⁶⁶ It can be seen that the ε_2 spectral shapes of the CTSe, CZTSe and CZTS are quite similar. The E_g values of CdTe and $\text{CH}_3\text{NH}_3\text{PbI}_3$ are reported to be 1.49 eV (Ref. 70) and 1.61 eV,⁶⁵ respectively.

Quite interestingly, all the light absorbers in Fig. 4(b) show similar α values near E_g ($\alpha \sim 1 \times 10^4 \text{ cm}^{-1}$), although the CZTSe and CTSe semiconductors indicate large α values exceeding 10^5 cm^{-1} at 2.0 eV. It can be seen that CdTe and $\text{CH}_3\text{NH}_3\text{PbI}_3$ absorbers exhibit quite sharp absorption tail, compared with the kesterite semiconductors. The density functional theory (DFT) analysis of CZTSe and CZTS shows that intermixing of constituent atoms occurs rather easily for the Cu, Zn and Sn atoms,^{71,72} which may contribute to generate the tail states in these semiconductors.

The earlier DFT studies reveal that the valence bands of the CZTSe (CZTS) are the anti-bonding states formed by the p - d hybridization of the Cu $3d$ and Se $4p$ (S $3p$)^{71,72} and this interaction pushes the valence band upward, reducing effective E_g ,^{73,74} as

observed in CIGS.⁶⁶ In contrast, when the Cu content is low, the weaker p - d interaction leads to the increase in E_g . In CZTSe and CZTS, therefore, E_g is expected to change with the Cu composition [$x = \text{Cu}/(\text{Zn} + \text{Sn})$]. For the fabrication of CZTSe and CZTS solar cells, a variety of the x values in a range of 0.77–0.86 (CZTSe)^{23,24,26-30} and 0.76–0.98 (CZTS)^{32,33,35-39} have been employed. However, the systematic variations of the CZTSe and CZTS dielectric functions with x have not been determined. Thus, we modeled the increase in E_g at low x by shifting the CZTSe and CZTS dielectric functions toward higher energy using ΔE_g as an energy-shift parameter. In this case, however, based on the well-known sum rule,⁷⁵ the relation of $\int E\varepsilon_2(E)dE = \text{const.}$ needs to be satisfied. Thus, if the ε_2 spectrum is shifted toward higher energy by ΔE_g , the ε_2 amplitude reduces by a factor of $f = E/(E + \Delta E_g)$ because $\int E\varepsilon_2(E)dE = \int (E + \Delta E_g)\varepsilon_2(E + \Delta E_g)dE$. Under these assumptions, the ε_2 spectrum of CZTSe layers can be expressed as

$$\varepsilon_2(E) = f\varepsilon_{2,\text{CZTSe}}(E - \Delta E_g) \quad (10)$$

In this equation, $\varepsilon_{2,\text{CZTSe}}$ shows the ε_2 spectrum of the CZTSe dielectric function in Fig. 4(a) ($\varepsilon_{\text{CZTSe}} = \varepsilon_{1,\text{CZTSe}} - i\varepsilon_{2,\text{CZTSe}}$) and the term of $-\Delta E_g$ shows the spectrum shift toward higher energy. In Eq. (10), we obtain $\varepsilon_2(E) = \varepsilon_{2,\text{CZTSe}}(E)$ when $\Delta E_g = 0$ eV. From the $\varepsilon_2(E)$ deduced from Eq. (10), the $\varepsilon_1(E)$ is obtained further using the Kramers-Kronig relations.⁵⁹ In this $\varepsilon_1(E)$ calculation, we used an ε_1 offset value of 0.770, estimated from the dielectric function modeling assuming the Tauc-Lorentz transitions.⁶¹ In Fig. 5, ε values calculated from our model using $\Delta E_g = 0.15$ and 0.30 eV are shown, together with $\varepsilon_{\text{CZTSe}}$ in Fig. 4(a) ($\Delta E_g = 0$ eV). The effect of the x in the CZTS can also be modeled by simply adopting the ε_2 spectrum of the CZTS ($\varepsilon_{2,\text{CZTS}}$) in Eq. (10), instead of $\varepsilon_{2,\text{CZTSe}}$.

On the other hand, when Se in CZTSe is replaced with S, E_g widening occurs by the upward shift of the conduction band and downward shift of the valence band.⁷⁶ As mentioned earlier, the overall shape of $\varepsilon_{\text{CZTSe}}$ is quite similar to that of $\varepsilon_{\text{CZTS}}$. In fact, when $\varepsilon_{2,\text{CZTSe}}(E)$ is slided toward higher energy, all the transition energies agree well with those of $\varepsilon_{2,\text{CZTS}}(E)$. Accordingly, to express the dielectric function of CZTSSe alloys, we employed the energy shift model in which the dielectric function of an arbitrary composition is “synthesized” from two known dielectric functions with different compositions.⁷⁷ When the CZTS _{y} Se _{$1-y$} dielectric function for an arbitrary S

composition [$y = S/(S + Se)$] is calculated by this model, $\varepsilon_{CZTSe}(E)$ is slid toward higher energy, while $\varepsilon_{CZTS}(E)$ is moved toward lower energy, so that the E_g position of these shifted spectra matches that of the target y composition. From these shifted dielectric functions, the dielectric function of the CZTSSe (ε_{CZTSSe}) is approximated as a weighted average of ε_{CZTSe} and ε_{CZTS} :

$$\varepsilon_{CZTSSe}(E) = (1 - y) \varepsilon_{CZTSe}(E_{\text{shift,Se}}) + y \varepsilon_{CZTS}(E_{\text{shift,S}}) \quad (11)$$

where $\varepsilon_{CZTSe}(E_{\text{shift,Se}})$ and $\varepsilon_{CZTS}(E_{\text{shift,S}})$ denote the CZTSe and CZTS dielectric functions obtained after the energy-shift adjustments.

In the energy region near E_g , $\varepsilon_{2,CZTSe}(E)$ overlaps with $\varepsilon_{2,CZTS}(E)$ when $\varepsilon_{2,CZTSe}(E)$ is shifted by 0.34 eV toward higher energy. Thus, we express the E_g position of the $CZTS_ySe_{1-y}$ as $E_g = 0.91 + 0.34y$ eV. In an ideal semiconductor alloy, E_g changes linearly with the alloy composition, but non-linear E_g variation (band gap bowing) also occurs in many semiconductor alloys. In CZTSSe, the effect of the band gap bowing has been reported to be small^{76,78,79} and this effect is neglected in our model. As a result, if the y value is selected, the E_g position is determined, and ε_{CZTSe} and ε_{CZTS} are shifted toward the target E_g value. From these shifted spectra, ε_{CZTSSe} is then calculated according to Eq. (11). Figure 6 shows ε_{CZTSSe} for different y values deduced from the energy shift model. The Cu contents of ε_{CZTSe} and ε_{CZTS} in Fig. 4 are $x = 0.95$ (CZTSe)⁶¹ and $x = 0.94$ (CZTS)⁶⁸ and thus the above model corresponds to ε_{CZTSSe} of $x \sim 0.95$. In CZTSSe, the reduction of x is also expected to shift the dielectric function toward higher energy, but this effect will be interpreted as an increase in the y composition.

As known well, the free carrier absorption in TCO materials, such as ZnO:Al and In_2O_3 :Sn (ITO), alters EQE spectra significantly and, for accurate EQE simulations, the free carrier absorption in the TCO layers needs to be expressed properly.¹⁹ Quite fortunately, the free carrier absorption in TCO layers can be described perfectly from the Drude model

$$\varepsilon_{\text{Drude}}(E) = -A_D/(E^2 - i\Gamma_D E), \quad (12)$$

where A_D and Γ_D are the amplitude and broadening parameters, respectively.⁵⁹ From these parameters, the optical carrier concentration (N_{opt}) and optical mobility (μ_{opt}) can be estimated from the relations of $A_D = \hbar^2 e^2 N_{\text{opt}} / (m^* \varepsilon_0)$ and $\Gamma_D = \hbar e / (m^* \mu_{\text{opt}})$.⁸⁰

Here, m^* is the effective mass. It should be noted that N_{opt} shows quite good agreement with the carrier concentration determined by the Hall measurement.⁸⁰ In contrast, μ_{opt} generally shows a much higher value than the mobility obtained from the Hall measurement, as μ_{opt} does not include the effect of grain boundary scattering.^{80,81} In the actual EQE analyses for reported spectra, the parameter values of A_D and Γ_D were

modified slightly in some cases to improve the EQE fitting. Moreover, in TCO layers, the E_g position shifts toward higher energy by the increase in N_{opt} (Burstein-Moss shift).^{80,82-84} Accordingly, in some analyses, the energy position of the TCO interband transition was also adjusted slightly by shifting the TCO dielectric function.

For the EQE analyses of CZTSe, CZTS, and CZTSSe solar cells, we employed the reported dielectric functions of non-doped ZnO,¹⁹ CdS,^{19,62} Mo,¹⁹ and MgF₂,¹⁹ while the free carrier absorption and the Burstein-Moss shift in ZnO:Al (Ref. 19), ZnO:Ga (Ref. 80) and ITO (Ref. 80) layers were modified slightly in some cases. For the MoSe₂ layer in CZTSe and CZTSSe solar cells, the dielectric function reported in Ref. 63 was used, whereas we employed a reported MoS₂ dielectric function⁸⁵ for CZTS solar cells.

We performed the EQE analysis of a CdTe solar cell⁴⁸ using the dielectric functions of CdTe (Fig. 4) and ITO (Ref. 80). For the MgF₂ and CdS layers incorporated into the CdTe solar cell, the dielectric functions mentioned above were employed. In addition, for the carbon rear electrode of the CdTe solar cell, we used the dielectric function of graphite.⁸⁶ In the EQE analyses of CH₃NH₃PbI₃ hybrid perovskite solar cells,^{49,50} on the other hand, the dielectric functions reported for CH₃NH₃PbI₃ (Fig. 4), SnO₂:F (Ref. 87), TiO₂ (Ref. 65) and Au (Refs. 86, 88) were employed.

IV. RESULTS

A. Analysis of CZTSe solar cells

Figure 7 shows the result of the EQE analysis performed for the CZTSe solar cell in Fig. 1 using the e-ARC method. For this calculation, the optical model of Fig. 2(b) was used. In Fig. 7, the experimental EQE spectrum is shown by the open circles and the calculated EQE spectrum obtained from the fitting analysis is indicated by the red line. The black lines represent the R_{tex} and A spectra obtained from the ARC method. In this analysis, the variation of x in the CZTSe layer is taken into account by employing ΔE_g . In Fig. 7, therefore, we carried out the EQE analysis using L_C in Eq. (5) and ΔE_g in Eq. (10) as free parameters.

In this CZTSe solar cell, A in the short λ region is limited essentially by the light absorption in the ZnO:Al and CdS layers. Specifically, the sharp reductions in the EQE response observed at $\lambda < 400$ nm and $\lambda < 540$ nm correspond to the onsets of strong light absorption in the ZnO:Al and CdS layers, respectively. The EQE reduction at $\lambda = 400$ –540 nm, induced by the CdS absorption, is governed primarily by the CdS thickness,¹⁹ and the CdS layer thickness estimated from the TEM image (70 nm) provides excellent fitting in Fig. 7. From the EQE spectra, the CdS layer thickness can

also be deduced rather easily.

The light absorption observed in the ZnO:Al at $\lambda > 450$ nm shows the contribution of free carrier absorption, which shows a notable increase at longer wavelengths.^{59,80} In CZTSe solar cells, the EQE at $\lambda = 600\text{--}1000$ nm is limited mainly by R_{tex} and the free carrier absorption. In Fig. 7, the Drude parameters of the ZnO:Al are $A_D = 0.869$ eV and $\Gamma_D = 0.111$ eV, which correspond to $N_{\text{opt}} = 1.8 \times 10^{20}$ cm⁻³ and $\mu_{\text{opt}} = 35.0$ cm²/(Vs), respectively. It has been reported that A_D of TCO layers changes depending on the underlying structure¹⁹ and total TCO thickness.⁸¹

In Fig. 7, the A spectrum of the CZTSe layer, shown as the yellow-colored region, corresponds to the EQE spectrum calculated within the ARC method ($L_C = \infty$), but the experimental EQE spectrum shows quite low values particularly in the long λ region. This result indicates the significant carrier loss within the CZTSe layer. In the analysis based on the e-ARC method, however, the calculated EQE spectrum provides excellent fitting to the experimental EQE spectrum when the parameter values of $L_C = 0.57$ μm and $\Delta E_g = 0.16$ eV are assumed. The J_{sc} value calculated from this analysis is 31.6 mA/cm² and agrees perfectly with the experimental value. The relatively large ΔE_g of 0.16 eV is induced by a low x of 0.82 used in the CZTSe absorber ($x = 0.95$ in Fig. 4). From the result of Fig. 7, the optical and recombination losses can be determined quantitatively.

In Fig. 7, the L_C value in the CZTSe (~ 0.6 μm) is much smaller than the total thickness of the CZTSe absorber layer (~ 1.3 μm), and the EQE in the longer λ region reduces by carrier recombination in the CZTSe bottom region. The limited carrier collection in CZTSe solar cells due to small L_D has been pointed out previously.^{15,16,23} In earlier studies on CZTSe solar cells, on the other hand, E_g of the CZTSe layers is often estimated from the EQE response in the longer λ region.²⁴⁻²⁷ Nevertheless, such analyses may lead to the overestimation of E_g if the EQE response in the longer λ regime is limited by the carrier collection, as confirmed from Fig. 7.

We also performed the EQE analysis by applying $H_2(\lambda)$ of Eq. (7). Figure 8 shows the results of the EQE fitting analyses for the CZTSe solar cell obtained using different $H(\lambda)$ functions and optical models. In this figure, the red and blue lines represent the EQE results for the analyses using $H_1(\lambda)$ and $H_2(\lambda)$, respectively. The experimental data (gray open circles) and the calculation result of $L_C = 0.57$ μm (red line) correspond to those in Fig. 7. As mentioned earlier, $H_1(\lambda)$ and $H_2(\lambda)$ are equivalent when $L_D = 0$. Thus, the EQE result obtained from $W = 0.57$ μm and $L_D = 0$ μm using $H_2(\lambda)$ is identical to that calculated from $L_C = 0.57$ μm using $H_1(\lambda)$. In the EQE analyses by $H_2(\lambda)$, however, the two fitting parameters (i.e., W and L_D) show a strong correlation and quite similar

spectra are obtained in a range of $W = 0.30\text{--}0.57 \mu\text{m}$ with $L_D = 0 \mu\text{m}$ ($W = 0.57 \mu\text{m}$) and $L_D = 0.50 \mu\text{m}$ ($W = 0.30 \mu\text{m}$). In particular, we found a relationship of $L_C \sim W + L_D/2$ between the parameters of L_C in $H_1(\lambda)$ and (W, L_D) in $H_2(\lambda)$. The reasonable fitting can also be obtained when the parameters of $W = 0 \mu\text{m}$ and $L_D = 1.5 \mu\text{m}$ are used, as shown in Fig. 8. Accordingly, it is rather difficult to determine W and L_D independently from the model of $H_2(\lambda)$, although the EQE fitting may improve slightly when these two parameters are employed in the analyses. The large correlation between W and L_D in the EQE analysis using $H_2(\lambda)$ has also been confirmed in our EQE analyses for CdTe and $\text{CH}_3\text{NH}_3\text{PbI}_3$ solar cells.

We also calculated the EQE spectrum by assuming that the total CZTSe thickness in the optical model is L_C ($d_{\text{CZTSe}} = 0.57 \mu\text{m}$) and this result is shown by the black line in Fig. 8. The overall trend of this EQE spectrum is similar to that obtained from $L_C = 0.57 \mu\text{m}$. In other words, L_C extracted from the EQE fitting analysis is roughly equivalent to the thickness of the absorber layer where the carrier extraction occurs predominantly. However, the absolute EQE values obtained from $d_{\text{CZTSe}} = 0.57 \mu\text{m}$ differ from those of $L_C = 0.57 \mu\text{m}$ in the long λ region due to the effects of the carrier recombination and the stronger back-side reflection in thinner layers.

To visualize the carrier generation and collection within the CZTSe solar cell, we further calculated partial A and EQE by dividing the CZTSe layer into 1-nm-thick sublayers, as implemented previously.¹⁹ In Fig. 9(a), partial A calculated for different depths from the CdS/CZTSe interface (d) and wavelengths is shown. The A values are normalized by the maximum value and the region of $d > 0.95 \mu\text{m}$ corresponds to the CZTSe/void region in Fig. 2(b). If the partial A spectrum obtained at different d is integrated, the A spectrum in Fig. 7 (yellow-colored region) can be obtained. The partial A value is quite high at $d \sim 0 \mu\text{m}$ and exhibits a rapid decay versus d due to the strong light absorption in the CZTSe layer. In the region of $\lambda > 900 \text{ nm}$, however, the light absorption and the resulting carrier generation occur rather uniformly throughout the entire CZTSe layer due to the lower α values in this region. The oscillation pattern observed in this region represents the weak interference effect induced by the thin film structure.

In Fig. 9(a), the $H_1(\lambda)$ values calculated from $L_C = 0.57 \mu\text{m}$ are also shown. By multiplying partial A by $H_1(\lambda)$, partial EQE within the CZTSe layer can be estimated [Fig. 9(b)]. If the partial EQE spectra in Fig. 9(b) are integrated, the EQE spectrum shown in Fig. 7 is obtained. The trends of partial A and partial EQE are essentially the same at $\lambda \leq 600 \text{ nm}$, since $H_1(\lambda) \sim 1$ in this region. In the longer λ region, however, the carrier collection is hindered strongly by the recombination in the bottom region and the

partial EQE reduces significantly. It should be emphasized that, at $\lambda \geq 900$ nm in Fig. 9(a), the holes and electrons generated near the CdS/CZTSe and CZTSe/MoSe₂ interfaces, respectively, need to travel the whole layer to generate the current in the device. Accordingly, short L_C lowers partial EQE particularly in the longer λ region.

In Fig. 9(c), partial EQE in the CZTSe layer is integrated toward the depth to deduce the contribution of partial EQE at each depth for J_{sc} . The J_{sc} profile obtained from partial A assuming $L_C = \infty$ is also shown in Fig. 9(c). It can be seen that the light absorption in the CZTSe occurs predominantly at $d < 200$ nm and J_{sc} increases rapidly in this thickness region. In particular, CZTSe shows a quite high α value exceeding 1×10^5 cm⁻¹ at 2.0 eV ($\lambda = 620$ nm) and the resulting penetration depth ($d_p = 1/\alpha$) is only ~ 100 nm. Thus, the rapid rise of J_{sc} up to 200 nm can be explained by the high α values in the CZTSe layer. In contrast, the increase in J_{sc} is smaller in the CZTSe bottom region, as the carrier collection in this region is limited by the enhanced recombination in this solar cell. Moreover, as indicated by the dotted line in Fig. 9(c), J_{sc} becomes almost constant in the region of $d \geq L_C$. The contribution of each λ for J_{sc} is also calculated for the cases of $L_C = \infty$ [Fig. 9(d)] and $L_C = 0.57$ μm [Fig. 9(e)]. When the L_C value is limited, the J_{sc} contribution from the longer λ region is lost and J_{sc} reduces by 6.5 mA/cm² in Fig. 9(e).

Figure 10 shows the normalized partial EQE of the CZTSe solar cell with $L_C = 0.57$ μm and this figure corresponds to partial EQE shown in Fig. 9(b). It can be confirmed from Fig. 10 that the light absorption at $\lambda < 700$ nm occurs predominantly near the CdS interface, whereas partial EQE is distributed uniformly toward the depth direction at $\lambda > 900$ nm. In the CZTSe solar cell, therefore, the carrier collection in this regime is quite important to gain sufficient J_{sc} .

By applying the e-ARC method, we have further analyzed the EQE spectra of various CZTSe solar cells fabricated by a coevaporation,^{23,26,27} a solution-based processing using hydrazine,²⁴ and a selenization process.²⁵ Figure 11 summarizes the experimental EQE spectra of the reported CZTSe solar cells (open circles) and the results of our EQE analyses (solid lines). The EQE analyses performed for these solar cells are essentially similar to that in Fig. 7; the thicknesses of the solar-cell component layers were extracted from the descriptions and the SEM images in each reference and, in the EQE fitting, L_C and ΔE_g of the CZTSe layers were varied. In the analyses, we also adjusted the TCO optical properties and the CdS thickness slightly. Although there is slight uncertainty for the TCO optical constants in the analyses of the reported EQE spectra, we confirmed that the TCO optical properties can still be deduced from the EQE response in the visible region ($\lambda \sim 600$ nm) and the accurate analysis of L_C is possible.

For the EQE analysis of Ref. 23, we employed the experimental R spectrum, instead of R_{tex} , to simplify the analysis. For the other EQE calculations, R_{tex} calculated from the ARC method was employed. As confirmed from Fig. 11, the e-ARC method provides excellent fitting to all the EQE spectra, independent of the detailed solar cell structure and processing method.

The EQE spectrum of Ref. 23 is obtained from a record-efficiency CZTSe solar cell with a conversion efficiency of 11.6% ($J_{\text{sc}} = 40.6 \text{ mA/cm}^2$, $V_{\text{oc}} = 423 \text{ mV}$, $FF = 0.673$). This solar cell has a very uniform thin film structure with large CZTSe grains and shows the highest L_C value of $2.3 \mu\text{m}$. As shown in Fig. 11, with decreasing the L_C value, the EQE response in the longer λ region reduces gradually and J_{sc} reduces from 40.6 mA/cm^2 (Ref. 23) to 27.0 mA/cm^2 (Ref. 27).

Other EQE spectra reported for CZTSe solar cells^{16,28-30} have also been analyzed by the e-ARC method and excellent fittings, similar to those in Fig. 11, have been obtained for these CZTSe solar cells. Figure 12 summarizes (a) J_{sc} , (b) V_{oc} and (c) efficiency of the CZTSe solar cells as a function of L_C estimated from our EQE analyses. From the ΔE_g obtained from each analysis, we calculated E_g of the CZTSe layer as $E_g = 0.91 + \Delta E_g \text{ eV}$. In Fig. 12, we categorized the analysis results into two groups depending on the E_g values of the CZTSe layers. In particular, the closed circles represent the analysis results for the CZTSe layers with relatively high E_g values in a range of 1.03–1.08 eV, whereas the closed squares show those with the lower E_g values ($E_g = 0.97\text{--}1.02 \text{ eV}$). The solid lines in Fig. 12(a) indicate the variations of J_{sc} with L_C , calculated assuming $E_g = 0.97 \text{ eV}$ (blue line) and 1.04 eV (red line) for the CZTSe absorber. For these simulations, we assumed the structure of Fig. 2(b) but with a uniform CZTSe layer ($2 \mu\text{m}$) without the CZTSe/void layer.

As confirmed from Fig. 12(a), simulated J_{sc} reproduces the experimental result quite well. The experimental J_{sc} value shows a higher value than simulated J_{sc} when (1) E_g of the CZTSe is lower, (2) the CZTSe layer is thicker, (3) the free carrier absorption in the TCO layer is smaller, and (4) the CdS layer is thinner, compared with our model structure. Quite interestingly, V_{oc} of the CZTSe solar cells is rather independent of L_C and, for the solar cells of $E_g = 1.03\text{--}1.08 \text{ eV}$, V_{oc} shows an upper limit of $\sim 425 \text{ mV}$ at $L_C = 0.6\text{--}2.3 \mu\text{m}$, as indicated by the dotted line in Fig. 12(b). When E_g is lower, on the other hand, V_{oc} reduces rather largely. Thus, CZTSe solar cells show higher performance when CZTSe layers with high E_g are formed by reducing the Cu content, as pointed out previously.⁸⁹ The variation of the conversion efficiency with L_C [Fig. 12(c)] is essentially governed by the change in J_{sc} , as V_{oc} is constant when E_g is high. For the further increase in the efficiency, the improvement of V_{oc} is crucial.

B. Analysis of CZTS and CZTSSe solar cells

We have further analyzed the EQE spectra of CZTS and CZTSSe solar cells by applying the e-ARC method. Figure 13 shows the EQE analysis results for (a) CZTS and (b) CZTSSe solar cells. In this figure, the open circles show the experimental spectra reported for CZTS (Refs. 31-35) and CZTSSe (Refs. 17, 40-43) solar cells, whereas the solid lines represent the calculated EQE spectra. The EQE analysis procedure in Fig. 13 is identical to that of CZTSe in Fig. 11, except that the dielectric functions of the CZTS and CZTSSe are applied in the analyses. As a result, the EQE fitting analyses for the CZTS solar cells were carried out using the two main parameters of L_C and ΔE_g .

The CZTS solar cells in Fig. 13(a) were fabricated by coevaporation³¹ and sulfurization processes.³²⁻³⁵ For these solar cells, the x values of 0.76–0.9 and the Zn/Sn ratios of 0.91–1.58 are applied,³²⁻³⁵ which result in the E_g values of 1.44–1.50 eV in our analyses. It can be seen from Fig. 13(a) that the e-ARC method provides excellent fitting to the EQE spectra of the CZTS solar cells and the EQE response in the longer λ region improves systematically with increasing L_C . The EQE spectrum of Ref. 31 is obtained from a high efficiency CZTS solar cell with a conversion efficiency of 8.4% ($J_{sc} = 19.5 \text{ mA/cm}^2$, $V_{oc} = 661 \text{ mV}$, $FF = 0.658$). The L_C values extracted from the CZTS solar cells are smaller than those of the CZTSe in Figs. 11 and 12. Moreover, at $\lambda = 500\text{--}600 \text{ nm}$, the experimental EQE values for Refs. 33 and 35 are slightly smaller, compared with the calculated EQE values, indicating that the carrier recombination occurs slightly near the CdS/CZTS interface.

The CZTSSe solar cells in Fig. 13(b) have been fabricated by a solution-based processing using hydrazine^{17,40} and selenization/sulfurization processes.⁴¹⁻⁴³ In the EQE analysis of these solar cells, $\varepsilon_{\text{CZTSSe}}$ was calculated from Eq. (11) and the EQE fitting was performed mainly by using the y composition of $\text{CZTS}_y\text{Se}_{1-y}$ and L_C . The E_g value of the $\text{CZTS}_y\text{Se}_{1-y}$ can then be calculated from the relation of $E_g = 0.91 + 0.34y \text{ eV}$ mentioned earlier. The excellent EQE fitting in the CZTSSe solar-cell analyses also confirms the validity of the e-ARC method and the variation of the EQE spectra can be reproduced almost perfectly by the change in L_C . In the CZTSSe solar cells with low L_C values,^{42,43} however, the EQE fitting deteriorates at $\lambda = 500\text{--}700 \text{ nm}$, indicating the presence of the recombination in the front interface region.

For the CZTSSe solar cells, the low y values of 0.25–0.40 and the Cu composition of $x = 0.8\text{--}1.0$ were employed with Zn/Sn ratios of 1.0–1.2.^{17,41-43} From the EQE analyses of these solar cells, we determined E_g of the CZTSSe layers to be 1.08–1.10 eV. The larger E_g values in the CZTSSe, compared with the CZTSe ($E_g = 0.91 \text{ eV}$), can be

interpreted by the high y and the low x values. In our dielectric function modeling of CZTSSe, however, the increase in E_g due to a low x is neglected and the E_g shift induced by the low x is compensated by the increase in y . Thus, in the actual EQE analyses for the CZTSSe, we obtained y values of 0.50–0.65, which are higher than the experimental y composition (0.25–0.40).^{17,42,43} The y values extracted from our EQE analyses are compared further with the reported (x, y) values, and we find that the E_g shift caused by the change in x (Δx) can be expressed as $\Delta E_g \sim 0.5\Delta x$ eV. Thus, the reduction in x from 0.9 to 0.8 (i.e., $\Delta x = 0.1$) increases E_g by ~ 50 meV.

We implemented similar EQE analyses for other CZTS solar cells³⁶⁻³⁹ and CZTSSe solar cells.⁴⁴⁻⁴⁷ Figure 14 summarizes (a) J_{sc} , (b) V_{oc} , (c) FF and (d) efficiency for all the CZTSe (Refs. 16, 23-30), CZTS (Refs. 31-39) and CZTSSe (Refs. 17, 40-47) solar cells analyzed in this study as a function of L_C extracted from the EQE analyses. The solid lines in this figure indicate the variations of J_{sc} with L_C , calculated assuming the E_g values of 1.04 eV (CZTSe), 1.08 eV (CZTSSe) and 1.46 eV (CZTS). For these simulations, we employed the structure of Fig. 2(b) with a uniform absorber layer (2 μm). Quite naturally, as E_g of the absorber material decreases, the overall J_{sc} value increases. The result for J_{sc} [Fig. 14(a)] indicates that the L_C values in the CZTS are smaller than those in the CZTSe and CZTSSe. Quite interestingly, for the variation of V_{oc} with L_C , CZTS shows the larger increase, compared with the CZTSe and CZTSSe. In particular, V_{oc} of the CZTSe is quite independent of L_C in a wide range and increases only slightly by 83 mV when L_C increases from 0.2 to 2.3 μm , whereas V_{oc} in the CZTS improves more than 184 mV in a similar L_C range. Accordingly, it appears that the limiting factors of V_{oc} in these solar cells are different.

In the CZTSe and CZTSSe solar cells, FF increases with increasing L_C . The low FF value in the CZTS solar cells suggests the lower quality of the CZTS absorber layers. It can be seen from Fig. 14(d) that, among the CZTSe, CZTS and CZTSSe solar cells, the CZTSSe shows the highest conversion efficiency. Although the L_C values of the CZTSe and CZTSSe layers are rather similar, the CZTSSe solar cell shows better performance due to higher V_{oc} . Furthermore, our analysis reveals that V_{oc} of the CZTSe and CZTSSe solar cells shows a weak correlation with E_g ; estimated E_g of the best performing CZTSe solar cell in Fig. 14(b) ($V_{oc} = 423$ mV, $L_C = 2.3$ μm for Ref. 23) is 1.07 eV, which is comparable to $E_g = 1.13$ eV obtained for the high efficiency CZTSSe solar cell ($V_{oc} = 513$ mV, $L_C = 0.75$ μm for Ref. 17). Thus, the incorporation of the S atoms appears to be effective in increasing V_{oc} , although analysis errors of ± 0.05 eV are expected for the E_g values deduced in our EQE analyses.

C. Analysis of a CdTe solar cell

We have analyzed the EQE spectrum of a reported CdTe solar cell that shows a conversion efficiency of 16.0% ($J_{sc}=26.1 \text{ mA/cm}^2$, $V_{oc} = 840 \text{ mV}$, $FF = 0.731$).⁴⁸ The structure of this device is $\text{MgF}_2/\text{glass}/\text{ITO} (200 \text{ nm})/\text{CdS} (50 \text{ nm})/\text{CdTe} (3.5 \text{ }\mu\text{m})/\text{carbon}$ electrode. The CdTe layer of this solar cell was processed by a standard close-spaced sublimation (CSS) method,^{90,91} followed by the aqueous CdCl_2 and the subsequent thermal-annealing ($420 \text{ }^\circ\text{C}$) treatments. In CdTe processes, the post CdCl_2 /annealing treatment is quite important to increase CdTe grain size and thus to reduce the carrier recombination at grain boundaries.⁹¹⁻⁹⁴ So far, a high conversion efficiency exceeding 20% has been reported for a CdTe-based solar cell,⁹⁵ although the structure of this device is not clear. It should be noted that only limited EQE analyses^{70,96-98} and optical simulations^{99,100} have been made for CdTe photovoltaic devices.

Figure 15 shows the result of the EQE analysis for the reported CdTe solar cell.⁴⁸ The shape of the experimental EQE spectrum (open circles) is essentially similar to those of the CZTSe and CZTS, although the longer λ response is limited in the CdTe solar cell due to larger E_g . In Fig. 15, the red line represents the EQE spectrum calculated from the e-ARC method, while the EQE spectrum of $L_C = \infty$ is indicated by the yellow-colored region. In this EQE analysis, the thicknesses of the ITO, CdS and CdTe layers were adopted from the description in Ref. 48, whereas the thickness of the anti-reflection MgF_2 layer was assumed to be 110 nm. In the EQE fitting analysis of Fig. 15, only L_C and the free carrier absorption in the ITO layer (i.e., A_D) were adjusted. We implemented optimization of the A_D value so that the EQE values at $\lambda = 600\text{--}700 \text{ nm}$ match the experimental values and, as a result, we obtained $A_D = 1.20 \text{ eV}$ with a fixed parameter of $\Gamma_D = 0.12 \text{ eV}$ [$N_{opt} = 2.8 \times 10^{20} \text{ cm}^{-3}$ and $\mu_{opt} = 29.5 \text{ cm}^2/(\text{Vs})$]. It can be seen that the calculated EQE spectrum agrees quite well with the experimental spectrum when $L_C = 1.1 \text{ }\mu\text{m}$. So far, for CdTe solar cells, the L_D values in a range of $0.4\text{--}3.7 \text{ }\mu\text{m}$ with $W = 0.2\text{--}5.5 \text{ }\mu\text{m}$ have been reported.^{96,97,101-103}

In Fig. 15, the experimental EQE is slightly smaller than the calculated EQE in a region of $\lambda = 520\text{--}570 \text{ nm}$, indicating the small carrier loss near the CdS/CdTe interface. It is now well established that the $\text{CdS}_x\text{Te}_{1-x}$ alloy is formed at the CdS/CdTe interface.^{90,92} Thus, the slight EQE reduction suggests the carrier recombination within the CdSTe phase. On the other hand, the disagreement at $\lambda > 850 \text{ nm}$ originates from the light absorption by the tail state. Although polycrystalline CdTe layers are expected to show strong tail absorption, we employed the CdTe dielectric function extracted from a single crystal⁶⁹ and the effect of the tail absorption was not considered in our analysis.

Quite surprisingly, L_C of the CdTe solar cell is comparable to that of the CZTSe solar

cells in Fig. 11 ($\sim 1 \mu\text{m}$), even though the carrier recombination loss in the CdTe solar cell is rather small (1.0 mA/cm^2 in Fig. 15). This effect can be understood based on partial EQE of the CdTe solar cell. Figure 16 shows (a) partial A for the ITO (200 nm)/CdS (50 nm)/CdTe ($3.5 \mu\text{m}$) and (b) partial EQE ($L_C = 1.1 \mu\text{m}$) for the CdTe device in Fig. 15. When the partial A values for the ITO, CdS and CdTe layers are integrated, those in Fig. 15 can be obtained, whereas partial EQE corresponds to the EQE spectrum in Fig. 15. In Fig. 16, the partial A and EQE values are normalized by the maximum values obtained in each layer. As shown in Fig. 16(a), the strong light absorption occurs below λ that corresponds to E_g of each layer. Nevertheless, in the CdTe layer, most of the light is absorbed in the region quite close to the CdS/CdTe interface due to the high α values above E_g . Accordingly, even when the L_C value is rather small ($L_C \sim 1 \mu\text{m}$), the major carrier loss occurs only in a narrow λ region of 800–850 nm. As a result, the influence of the carrier recombination is suppressed quite well in the case of the CdTe solar cell. This result represents the quite important phenomenon in photovoltaic devices; namely, carrier recombination dynamics are affected significantly by the α spectrum of a light absorber layer and the recombination loss within the bulk component reduces if $\alpha(\lambda)$ shows high values with sharp absorption edge. In this sense, $\alpha(\lambda)$ of CdTe has a more ideal shape, if compared with CZTSe and CZTS.

D. Analysis of $\text{CH}_3\text{NH}_3\text{PbI}_3$ solar cells

To study the working principles of hybrid perovskite solar cells, the optical and recombination losses in reported $\text{CH}_3\text{NH}_3\text{PbI}_3$ solar cells^{49,50} were determined using the e-ARC method. In particular, we have analyzed the EQE spectra of the $\text{CH}_3\text{NH}_3\text{PbI}_3$ solar cells with and without an hole transport layer (HTL) to elucidate the effect of the HTL on the carrier recombination.

Figure 17 shows the optical models for $\text{CH}_3\text{NH}_3\text{PbI}_3$ solar cells (a) with an HTL (Ref. 49) and (b) with no HTL (Ref. 50), and the corresponding EQE analysis results are shown in (c) and (d), respectively. The solar cell in Fig. 17(a) has a structure of glass/ SnO_2 :F/ TiO_2 / $\text{CH}_3\text{NH}_3\text{PbI}_3$ /polytriarylamine(PTAA)/Au. In this device, the PTAA layer corresponds to the HTL. In more conventional $\text{CH}_3\text{NH}_3\text{PbI}_3$ solar cells, mesoporous TiO_2 layers are inserted between the uniform (compact) TiO_2 and $\text{CH}_3\text{NH}_3\text{PbI}_3$ layers.¹⁰⁴⁻¹⁰⁷ However, for the $\text{CH}_3\text{NH}_3\text{PbI}_3$ solar cell of Fig. 17(a), a new spin-coating process allows the removal of the mesoporous TiO_2 layer and a high efficiency of 17.6 % has been obtained ($V_{oc} = 1.1 \text{ V}$, $J_{sc} = 20.5 \text{ mA/cm}^2$ and $\text{FF} = 0.78$).⁴⁹ For this solar cell, the optical modeling becomes quite simple because of a flat device structure.

In the optical model of Fig. 17(a), a complicated structure of SnO₂:F/SiO₂/SnO₂/glass (TEC-8, Pilkington) has been simplified to a SnO₂:F (600 nm)/glass structure. The validity of this approximation has been confirmed previously.⁶⁵ From the SEM image reported in Ref. 49, the thicknesses of the compact TiO₂ and CH₃NH₃PbI₃ layers were determined to be 30 nm and 300 nm, respectively. Unfortunately, for the PTAA layer, the optical constants have not been reported. However, the PTAA shows light absorption only in a high energy region of $E \geq 2.9$ eV,¹⁰⁸ which is notably larger than $E_g = 1.61$ eV of CH₃NH₃PbI₃. In the device, therefore, the light absorption within the PTAA is essentially negligible. In fact, spiro-OMeTAD [2,2',7,7'-tetrakis-(*N,N*-di-*p*-methoxyphenylamine)9,9'-spirobifluorene], which is used widely as an HTL of hybrid perovskite solar cells,¹⁰⁵⁻¹⁰⁷ shows the same absorption onset at $E = 2.9$ eV,^{65,109} and the optical loss in this layer is confirmed to be quite small.⁶⁵ Accordingly, in our optical model, the thickness of the PTAA layer is assumed to be zero. It should be emphasized that, when the EQE is calculated by incorporating a spiro-OMeTAD layer as an HTL, we observed no major changes. Thus, the influence of the HTL on the EQE spectrum is quite minor.

For the EQE analysis of the CH₃NH₃PbI₃ solar cells, we further assumed the carrier recombination in the TiO₂/CH₃NH₃PbI₃ interface region. This recombination is modeled by simply dividing a CH₃NH₃PbI₃ bulk layer into two layers and treating a thin layer located at the TiO₂ interface as a “dead layer” that allows no carrier extraction [see Fig. 17(a)].

In Fig. 17(c), the A spectra of each solar-cell component layer calculated using the optical model of Fig. 17(a) are shown. In this figure, R_{tex} deduced using the ARC method is also indicated. The yellow-colored region in Fig. 17(c) represents the A spectrum of the CH₃NH₃PbI₃, and the hatched-line region corresponds to the A component of the dead (recombination) layer near the TiO₂. We found that the calculated EQE (red line) shows good agreement with the experimental result (open circles) when the thickness of the dead layer is 4 nm with $L_C = \infty$. This result indicates clearly that the dominant recombination within the CH₃NH₃PbI₃ solar cell occurs near the TiO₂/CH₃NH₃PbI₃ interface region and the carrier loss near the HTL interface is negligible. Although the thickness of the front dead layer is thin (4 nm), the recombination loss by this layer leads to the reduction of J_{sc} by 0.9 mA/cm². The carrier recombination near the TiO₂ interface region has also been suggested in our previous study.⁶⁵

In Fig. 17(c), on the other hand, the agreement between the experimental and calculated EQE spectra is rather poor at $\lambda = 720\text{--}800$ nm. The deviation of the

calculated spectrum in this region is caused primarily by calculation errors of R_{tex} . Specifically, when the layer thickness of solar cells is thin, the period of the optical interference versus λ becomes larger. In this case, when the minimum positions in the calculated R_{flat} spectrum are simply connected, experimental R cannot be reproduced accurately in the E_g region where R shows the sharp increase due to the negligible light absorption at $E < E_g$. In fact, at $\lambda = 750$ nm in Fig. 17(c), R_{tex} almost overlaps with experimental EQE (i.e., $R_{\text{tex}} + EQE \sim 100\%$), which is not possible due to the light absorption within the SnO₂:F and Au layers. The above problem can be avoided if the experimental R spectrum obtained from an actual solar cell is used in Eq. (4). In Fig. 17(c), however, the error in the R_{tex} calculation affects J_{sc} only slightly (0.4 mA/cm²) and the quantitative analysis can still be made.

The solar cell with no HTL shown in Fig. 17(b) has a structure of glass/SnO₂:F/compact TiO₂/mesoporous TiO₂-CH₃NH₃PbI₃/CH₃NH₃PbI₃/Au.⁵⁰ As reported previously,⁶⁵ the optical response within the mesoporous TiO₂-CH₃NH₃PbI₃ mixed-phase layer can be expressed by the two separate flat layers of the TiO₂ and CH₃NH₃PbI₃. In the optical model of Fig. 17(b), the TiO₂ volume fraction within the mesoporous layer is assumed to be 30% (porosity 70%), which is consistent with the porosity of 58-64% reported in earlier studies.^{110,111} With this assumption, the thicknesses of the component layers were determined based on the SEM image of the solar cell and the description in Ref. 50. However, minor adjustments were made for the layer thicknesses in the actual analysis, and the layer thicknesses used in our EQE analysis are summarized in Fig. 17(b).

Figure 17(d) shows the result of the EQE analysis performed for the CH₃NH₃PbI₃ solar cell with no HTL. The experimental EQE spectrum of this solar cell (open circles) is quite different from that of the CH₃NH₃PbI₃ solar cell with the HTL; the overall EQE values are smaller and the EQE response in the longer λ region reduces significantly. The EQE spectra similar to that in Fig. 17(d) have been reported for CH₃NH₃PbI₃ solar cells that have no HTL layers.¹¹²⁻¹¹⁵

The yellow-colored region in Fig. 17(d), which corresponds to A of the CH₃NH₃PbI₃ layer, is essentially the same with that in Fig. 17(c), as the device structures are quite similar. However, the A spectra of the TiO₂ and SnO₂:F layers change slightly as the TiO₂ thickness is thicker and the SnO₂:F thickness is thinner in Fig. 17(d). The red line in Fig. 17(d) represents the EQE spectrum calculated assuming the carrier recombination in the front and rear interface regions. From the EQE values in the short wavelength region, the thickness of the front recombination layer is determined to be 10 nm and the EQE reduction caused by this layer is indicated by the hatched-line region.

For EQE in the longer λ region, we obtained the good fitting when $L_C = 280$ nm. The result of Fig. 17 indicates clearly that the presence of an HTL modifies the carrier recombination within the $\text{CH}_3\text{NH}_3\text{PbI}_3$ significantly.

Figure 18 shows partial EQE obtained at different depths from the $\text{TiO}_2/\text{CH}_3\text{NH}_3\text{PbI}_3$ interface in the $\text{CH}_3\text{NH}_3\text{PbI}_3$ solar cells (a) with the HTL and (b) with no HTL. These partial EQE values correspond to the EQE spectra shown as the red lines in Figs. 17(c) and 17(d), and the partial EQE values are normalized by the maximum values in each solar cell. It can be seen that, at $\lambda < 500$ nm, the light absorption and the resulting carrier generation occur in the region close to the $\text{TiO}_2/\text{CH}_3\text{NH}_3\text{PbI}_3$ interface. Accordingly, the presence of the dead layer near the TiO_2 interface reduces the short λ response greatly even if the thickness of the dead layer is thin, as evidenced from the hatched regions in Figs. 17(c) and 17(d).

In the longer λ region of 600–800 nm, on the other hand, the carrier generation occurs rather uniformly toward the depth due to the relatively low α values in this region. In this case, the photocarriers generated at the front and rear interfaces need to travel the distance that corresponds to the whole $\text{CH}_3\text{NH}_3\text{PbI}_3$ thickness. The good agreement between the experimental and calculated EQE at $\lambda > 600$ nm, observed for the $\text{CH}_3\text{NH}_3\text{PbI}_3$ solar cell with the HTL [Fig. 17(c)], ensures the long carrier diffusion length, which is at least comparable to the $\text{CH}_3\text{NH}_3\text{PbI}_3$ layer thickness.⁶⁵ When the HTL is not present, however, the collection of carriers is hindered strongly and partial EQE in the longer λ region reduces. The results of Fig. 18 confirm that the effect of the carrier recombination within the $\text{CH}_3\text{NH}_3\text{PbI}_3$ layer appears primarily as the EQE response at $\lambda > 600$ nm.

V. DISCUSSION

A. Optical and recombination losses

Figure 19 summarizes the experimental EQE spectra for various solar cells: CZTSe (Fig. 7), CZTSSe [Ref. 17 in Fig. 13(b)], CIGSe (Ref. 19), CZTS [Ref. 31 in Fig. 13(a)], CdTe (Ref. 48 in Fig. 15) and $\text{CH}_3\text{NH}_3\text{PbI}_3$ [Ref. 49 in Fig. 17(c)]. In Fig. 19, the reduction of EQE at $\lambda = 400$ –540 nm, caused by the parasitic absorption in the CdS layers, is observed in all the solar cells, except for the $\text{CH}_3\text{NH}_3\text{PbI}_3$ solar cell. The EQE response in the longer λ region is determined by E_g , but reduces when the recombination is present. In each EQE spectrum, the maximum EQE in the visible region is essentially governed by the light reflection and the free carrier absorption in the front TCO. By providing an anti-reflection layer and suppressing the free carrier

absorption, high EQE values of ~95% can be achieved, as shown in Fig. 19.

Figure 20 illustrates the optical and recombination losses deduced from our EQE analyses performed for the spectra shown in Fig. 19: (a) CIGSe, (b) CZTSe, (c) CZTSSe, (d) CZTS, (e) CdTe, and (f) CH₃NH₃PbI₃. In this figure, the numerical values represent the corresponding current densities in units of mA/cm². The maximum J_{sc} value attainable under AM1.5G condition is also calculated from the λ position of the absorption edge in each absorber layer, and the optical gain indicated in Fig. 20 represents the ratio of output J_{sc} divided by the maximum attainable J_{sc} value. The J_{sc} contributions obtained assuming two sublayers (top and bottom layers) with an equal thickness are also indicated. For the CIGSe, the result is adopted from our earlier EQE analysis.¹⁹ This CIGSe solar cell is fabricated by the three-stage coevaporation process and has a standard structure of MgF₂ (130 nm)/ZnO:Al (360 nm)/non-doped ZnO (50 nm)/CdS (45 nm)/CIGSe (1.8 μ m)/MoSe₂ (10 nm)/Mo/soda-lime glass with a conversion efficiency of 16.7% (J_{sc} = 34.2 mA/cm², V_{oc} = 674 mV, FF = 0.725).

In Fig. 20, the CIGSe and CdTe solar cells show high optical gains of ~80%, whereas the optical gains of the CZTSe, CZTSSe, CZTS, and CH₃NH₃PbI₃ solar cells are in a range of 51–70%. The optical losses in these solar cells can mainly be categorized by (1) the reflection loss, (2) the free carrier absorption in the front TCO, (3) the parasitic absorption in the CdS dead layer, and (4) the strong light absorption by the Mo back contact. The reflection loss increases when E_g of an absorber layer is low, as the EQE spectral range becomes wider and the integrated reflection loss increases in this case. More specifically, the reflection losses in the CZTSe and CZTSSe solar cells ($E_g \sim 1.0$ eV) are 2.5–4.5 mA/cm², which are apparently larger than those in the CZTS and CdTe solar cells. The CH₃NH₃PbI₃ solar cell also shows a large reflection loss (3.2 mA/cm²) due to the lack of an anti-reflection coating and the thin absorber-layer thickness (~300 nm).

The parasitic absorption by front TCO layers is a common problem for all thin-film solar cells. The optical loss in a front TCO layer tends to increase in solar cells having low- E_g absorbers due to the widening of the EQE spectral range. Moreover, the free carrier absorption in TCO layers increases drastically at longer wavelengths.^{59,80} Accordingly, when low- E_g absorbers are applied, the suppression of reflection loss and absorption loss in the front TCO becomes critical in achieving high conversion efficiencies. The Al-doped ZnO layers generally show a low N_{opt} value of $\sim 2 \times 10^{20}$ cm⁻³ [$\mu_{opt} = 30\text{--}50$ cm²/(Vs)]^{19,81} and the typical thickness of the ZnO:Al (~300 nm) results in the absorption loss of ~3 mA/cm² [see Figs. 20(a) and 20(b)]. In the CZTSSe solar cell in Fig. 20(c), the TCO absorption is suppressed by incorporating a thin ITO layer

(50 nm).¹¹⁶ In the CdTe solar cell, the optical loss caused by the front ITO is only 0.7 mA/cm² even though the ITO thickness is 200 nm. This small optical loss in the front TCO originates from the large E_g value of CdTe, which limits the effect of the free carrier absorption. In contrast, the CH₃NH₃PbI₃ solar cell having a larger E_g value shows the relatively large front TCO loss. This is caused by strong free carrier absorption originating from a thick TCO layer (600 nm) with a high N_{opt} of 5×10^{20} cm⁻³ (TEC glass).^{117,118} As reported previously,¹¹⁹⁻¹²¹ the parasitic light absorption in the front TCO can be reduced by employing high-mobility TCO layers, which exhibit quite low free carrier absorption.

The optical loss induced by the CdS layer (~50 nm) is ~3 mA/cm², as observed for CIGSe, CZTSe, CZTS and CdTe solar cells in Fig. 20. In the CZTSSe solar cell [Fig. 20(c)], the optical loss in the CdS is reduced by incorporating a quite thin CdS layer (25 nm).¹¹⁶ In high-efficiency CdTe solar cells, the parasitic absorption in the CdS layer is also reduced by adopting a thin layer.^{94,122} In conventional CdTe solar cells, however, V_{oc} shows a sharp reduction when the CdS thickness is reduced below 60 nm.^{94,122} Quite fortunately, it has been found that such V_{oc} reduction can be suppressed by incorporating a high-resistive TCO layer at the front TCO/CdS interface.^{94,122} In a record efficiency CdTe-based solar cell (21.5%), the parasitic absorption in the CdS-absorption region is suppressed quite well.⁹⁵

In the CIGSe and CZT(S)Se solar cells, a strong optical loss occurs by the parasitic absorption in the Mo layer. This effect can be attributed to the inherent problem of Mo: i.e., low reflectivity of Mo particularly in the longer λ region.^{19,123-125} The strong parasitic absorption in the Mo is evident in the EQE analysis result for the CZTSe solar cell (Fig. 7). The optical loss induced by the Mo increases when a thinner absorber is employed, as confirmed for the CZTS solar cell in Fig. 20(d). For CIGSe solar cells, the application of highly reflective metals, such as Au, Ag, Cu and Al, has been rather difficult in part due to a high processing temperature of the CIGSe absorber, although Au back electrodes have been employed for CIGS solar cells fabricated by a lift-off process.¹²⁵ For CIGSe and CZT(S)Se solar cells, the formation of more ideal back-reflector structures is preferable for the further increase in J_{sc} .

In all the solar cells, the J_{sc} contribution of the top sublayer is significant, compared with that of the bottom sublayer. In the CdTe solar cell, the J_{sc} contribution of the bottom sublayer is quite small due to the strong light absorption within the CdTe absorber layer, as confirmed from Fig. 16(a). Thus, the thickness of the CdTe layer could be reduced down to ~1 μ m without deteriorating the efficiency to lower the production cost. However, the backside recombination may influence the performance

in this case (see Sec. V B). In the case of the $\text{CH}_3\text{NH}_3\text{PbI}_3$ solar cell, however, J_{sc} generated in the bottom region is still important due to the thin thickness of the $\text{CH}_3\text{NH}_3\text{PbI}_3$ absorber. It should be emphasized that the $\text{CH}_3\text{NH}_3\text{PbI}_3$ solar cell shows quite small overall optical losses. In particular, the parasitic absorption within the TiO_2 and HTL layers is negligible and the major optical loss occurs only in the front TCO layer, which can be optimized further. Thus, a quite high conversion efficiency reported for $\text{CH}_3\text{NH}_3\text{PbI}_3$ solar cells ($\sim 20\%$) can be understood partly by the low parasitic absorption within the solar-cell component layers.⁶⁵

B. Carrier recombination

Although our model for the carrier recombination is extremely simple, almost all the EQE spectra reported for CZTSe, CZTS, CZTSSe, CdTe and $\text{CH}_3\text{NH}_3\text{PbI}_3$ solar cells can be analyzed using the identical formula of $H_1(\lambda)$. In some cases, however, the model of $H_1(\lambda)$ may not be appropriate, and such limitations need to be clarified further. Unfortunately, our EQE analyses performed for various solar cells do not allow the determination of the recombination mechanism, but our analyses provide the quantitative results for (1) the total J_{sc} loss induced by the carrier recombination and (2) the thickness region where the carrier loss occurs predominantly (i.e., near front or rear interface region). As mentioned above, L_C extracted from the e-ARC method is a reference value and does not correlate directly with L_D and W . Accordingly, we emphasize that the discussion concerning recombination mechanisms described here is qualitative.

Our EQE analyses reveal that the recombination losses are well suppressed in CdTe and $\text{CH}_3\text{NH}_3\text{PbI}_3$ solar cells, while the CZTSe and CZTSSe solar cells show relatively large recombination losses. On the other hand, state-of-the-art CIGSe solar cells show almost 100% carrier collection with negligible carrier recombination.¹⁹ The recombination losses in the various solar cells of Fig. 20 can be interpreted by the corresponding band diagrams. Figure 21 summarizes the schematic band diagrams of (a) CIGSe, (b) CZTSe, (c) CdTe and (d) $\text{CH}_3\text{NH}_3\text{PbI}_3$ solar cells. These diagrams are drawn by referring to those reported earlier for CIGSe solar cells,¹²⁶⁻¹³⁰ CZTSe solar cells,¹³¹⁻¹³⁴ and CdTe solar cells,^{98,135-137} whereas the band diagrams of $\text{CH}_3\text{NH}_3\text{PbI}_3$ solar cells in Fig. 21(d) represent those proposed in this study. For the CIGSe and CZTSe solar cells, however, the band diagram near the MoSe_2 is not shown, as the band diagram at the MoSe_2 rear interface remains controversial.^{129,138} In Fig. 21, the band diagrams are shown by using a consistent energy scale, and the rough scales of L_C , L_D and W are also indicated. The carrier recombination processes that occur in the rear

interface, bulk and front interface regions are also illustrated as *A*, *B*, and *C* in Fig. 21, respectively.

As known well, the CIGSe, CZTSe and CdTe exhibit *p*-type conductivity and the depletion region, formed with the *n*-type CdS, extends deeper into the *p*-type absorber layers.¹²⁶⁻¹³⁷ In CIGSe and CZTSe solar cells, the conduction band offset (ΔE_C) at the CdS/non-doped ZnO is 0.2 eV.^{128,130,133,134} In the case of CIGSe solar cells, to suppress the carrier recombination at both front and rear interfaces, the V-shaped Ga profile is generally formed toward the growth direction by a three-stage process, in which Cu, In, Ga and Se elemental sources are supplied with different sequences.¹³⁹⁻¹⁴¹ In the resulting CIGSe layer, E_g (Ga content) is low at the valley position, typically located at 0.5 μm from the CdS/CIGSe interface,^{19,142} while E_g increases toward the front and rear interfaces. In CIGSe alloys, the energy position of the conduction band minimum (CBM) shifts upward with increasing the Ga content.^{143,144} Thus, the V-shaped Ga profile predominantly modifies the CBM position. In the band diagram of Fig. 21(a), the Ga-profile of the actual CIGSe solar cell [Fig. 20(a)] is reproduced and ΔE_C at the CdS/CIGSe interface becomes zero when a Ga composition at the front interface is 40 %.¹⁴⁵ Moreover, from the E_g values at the valley and rear positions, the conduction band barrier is estimated to be 0.14 eV.¹⁹ Although this barrier height is rather small, the pseudo-potential generated by the Ga-grading suppresses the rear-interface recombination quite effectively.^{127,129,140,141,146} Moreover, the light absorption in the CIGSe layer ($\sim 2 \mu\text{m}$) occurs primarily in the 1- μm -thick region from the CdS/CIGSe interface. From this result, we concluded previously that the CIGSe bottom layer (1 μm) with higher Ga contents plays a dominant role as a back-surface field (BSF) layer.¹⁹

In CZTSe solar cells [Fig. 21(b)], on the other hand, a quite large ΔE_C value at the CdS/CZTSe interface (0.48–0.6 eV) has been reported.^{131,132} Moreover, in this solar cell, the flat-band formation is expected to occur as no intentional composition modulation is made within the CZTSe layer. Earlier studies on CZTSe and CIGSe solar cells show that the hole carrier concentration (N_p) of a CZTSe layer is $3 \times 10^{16} \text{ cm}^{-3}$ with $W = 0.2 \mu\text{m}$, which are comparable to the values of $N_p = 2 \times 10^{16} \text{ cm}^{-3}$ and $W = 0.4 \mu\text{m}$ in a CIGSe.¹⁴⁷ In fact, in the device simulations for CIGSe^{130,148} and CZTSe^{133,134} solar cells, N_p of $\sim 1 \times 10^{16} \text{ cm}^{-3}$ is generally assumed. Consequently, the W values of the CIGSe and CZTSe solar cells are similar. Accordingly, the large difference in L_C between the CIGSe ($L_C = \infty$) and CZTSe ($L_C = 0.57 \mu\text{m}$ in Fig. 7) is likely caused by the variation in L_D , as illustrated in Figs. 21(a) and 21(b).

There are two possible recombination passes that are expected to lower L_D in CZTSe solar cells: i.e., the recombination (1) at the CZTSe/MoSe₂ interface and (2) within the

CZTSe bulk layer [i.e., *A* and *B* in Fig. 21(b)]. Unfortunately, from our EQE analyses, these recombination passes cannot be distinguished. However, since there is no BSF structure in CZTSe solar cells, the carrier recombination at the rear interface is possible. Moreover, in CZTS solar cells, the phase separation of CZTS into the Cu₂SnS₃ (CTS) and ZnS components occurs at the CZTS/MoS₂ rear interface.¹⁴⁹ This result implies that the formation of the CTSe and ZnSe secondary phase may also occur at the CZTSe/MoSe₂ interface. Since CTS and CTSe have lower E_g values, compared with the CZTS and CZTSe, respectively, such compositional change likely leads to the severe recombination. The low V_{oc} value in the CZTSe solar cells, which is independent of L_C [see Fig. 14(b)], also suggests the interface-limited performance of CZTSe solar cells. In fact, when a TiN barrier layer is provided on the Mo substrate, the EQE response in the longer λ region and the PL life time improve significantly.⁵⁴

However, the possibility of the intense carrier recombination in the CZTSe grain boundary region cannot be ruled out. In particular, the high-resolution compositional analysis performed for CZT(S)Se layers revealed the higher Cu contents in the grain boundary region,^{24,149} which likely enhance the CT(S)Se formation. Although scanning-probe microscopy (SPM) measurements confirm the enhanced carrier extraction from the grain boundary region in CZTSSe layers,¹⁵⁰ the formation of larger CZTSe grains has been quite effective in improving L_C .²³ Accordingly, it appears that the performance of the CZTSe solar cells is limited by intense carrier recombinations in both bulk and rear interface regions. Just recently, however, from bias-voltage-dependent EQE analyses and simulations, it has been reported that the carrier recombination in CZTSe¹⁸ and CZTSSe¹⁵¹ solar cells occurs predominantly at the band tail states and the conversion efficiency of the CZTSe-based solar cells is limited essentially by the formation of the tail states.^{18,151}

In CdTe solar cells [Fig. 21(c)], on the other hand, the Fermi level (E_F) in the CdS layers locates near the CBM^{98,135-137} and the CdS/CdTe interface shows the cliff-type discontinuity ($\Delta E_C = 0.2$ eV)¹⁵² due to larger E_g of CdTe. For *p*-type CdTe layers, there have been no simple metal electrodes that provide ohmic contacts and the carbon electrode with excessive Cu is used as a rear electrode. The presence of the Cu atoms is important to lower the height of the Schottky barrier formed at the CdTe/C interface,¹³⁵ although the extensive diffusion of the Cu atoms into the CdTe absorber limits the stability of the devices.^{135,153,154} It has been confirmed that the presence of the Schottky barrier at the CdTe rear interface reduces the current in the forward bias region.¹³⁶

For CdTe solar cells, CdTe layers with a low N_p value of 10^{14} – 10^{15} cm⁻³ have been applied.^{98,136,137} This N_p value is much lower than those of the CIGSe and CZTSe (N_p

$\sim 10^{16} \text{ cm}^{-3}$). As a result, the depletion region in the CdTe extends far deeper into the CdTe layer ($W = 1\text{--}3 \text{ }\mu\text{m}$),^{137,155} if compared with the CIGSe and CZTSe solar cells. In the CdTe solar cells, however, the light penetration at $\lambda < 800 \text{ nm}$ occurs within $1 \text{ }\mu\text{m}$ from the CdS/CdTe interface due to the high α values, as shown in Fig. 16(a). Accordingly, in the case of CdTe solar cells, most of the carriers are generated within the thick depletion region and the electric-field-assisted carrier collection occurs,^{137,155} which is quite beneficial to increase the EQE response at longer λ . As a result, we observe $L_C \sim W$ in CdTe solar cells, whereas the relation of $L_C > W$ is confirmed for CIGSe and CZTSe solar cells. Thus, the contribution of L_D is considered to be more important in the CIGSe and CZT(S)Se solar cells. In the CdTe solar cells, however, low N_p leads to a small E_F shift within the CdTe layer, which in turn reduces the built-in potential.^{137,156} In fact, for the CdTe solar cell in Fig. 20(e), the V_{oc} loss, defined by $V_{loss} = E_g/e - V_{oc}$, is 650 mV and this V_{loss} is larger than those observed in the CIGSe ($V_{loss} = 451 \text{ mV}$)¹⁹ and $\text{CH}_3\text{NH}_3\text{PbI}_3$ (510 mV)⁴⁹ solar cells. On the other hand, the high-efficiency CZTSe,²³ CZTSSe,¹⁷ and CZTS (Ref. 31) solar cells show V_{loss} values of 647, 617 and 799 mV, respectively, if the E_g values obtained from our EQE analyses are applied. To suppress the V_{oc} loss in CdTe solar cells, the introduction of a ZnTe BSF layer at the CdTe/C interface has been proposed^{137,157,158} and performed.^{159,160} The recombination loss of 1.0 mA/cm^2 in the CdTe bottom region could also be eliminated by providing the ZnTe BSF layer at the rear interface.¹⁵⁷

For CdCl_2 -treated CdTe solar cells, the effective carrier collection from the grain boundary region has been confirmed from EBIC^{2,161,162} and scanning capacitance microscopy.^{163,164} Nevertheless, earlier studies on CdTe solar cells pointed out that V_{oc} is still limited by the leakage current in the grain boundary region.^{164,165} Indeed, in a single-crystal CdTe solar cell, a quite high V_{oc} value of 929 mV ($V_{loss} = 561 \text{ mV}$) has been obtained at a similar N_p value of $\sim 6 \times 10^{15} \text{ cm}^{-3}$.¹⁵⁶ Thus, for the increase in V_{oc} of CdTe solar cells, the formation of larger grain is important, in addition to high N_p . In the CIGSe, the growth of large grains ($1\text{--}2 \text{ }\mu\text{m}$) has been realized by utilizing a liquid Cu-Se phase generated during the three-stage process,¹⁴⁰ whereas the grain size in the CZTSe has been improved by NaF post treatments.²³ Accordingly, in CIGSe, CZTSe and CdTe solar cells, the suppression of the grain boundary formation has been critical to obtain higher efficiencies.

In Fig. 21(d), the band diagrams for $\text{CH}_3\text{NH}_3\text{PbI}_3$ solar cells with an HTL (spiro-OMeTAD) and with no HTL are shown. The ΔE_C value at the $\text{TiO}_2/\text{CH}_3\text{NH}_3\text{PbI}_3$, determined from the direct and inverse photoemission spectroscopies, is $\sim 0.1 \text{ eV}$,^{166,167} and E_F of the TiO_2 locates near the CBM¹⁶⁶ due to a high carrier concentration of 10^{19}

cm⁻³ in this layer.¹⁶⁸ For the spiro-OMeTAD in Fig. 21(d), the energy positions of the highest occupied molecular orbital (HOMO) and lowest unoccupied molecular orbital (LUMO) are shown with an energy separation that corresponds to E_g (2.9 eV).⁶⁵ When the spiro-OMeTAD is doped with Li, E_F shifts toward the HOMO,¹⁶⁹ and the energy difference between the HOMO of the Li-doped spiro-OMeTAD and the valence band maximum of CH₃NH₃PbI₃ is reported to be ~0.2 eV from the ultraviolet photoelectron spectroscopy (UPS).¹⁶⁷ In Fig. 21(d), the energy offsets at the front and rear interfaces of the CH₃NH₃PbI₃ are reproduced by using the above experimental values. It can be seen that, in CH₃NH₃PbI₃ solar cells, the electrons and holes generated within the absorber layer are collected in the front and rear electrodes without any potential barriers.¹⁰⁵

Unfortunately, for the electric-field distribution within the CH₃NH₃PbI₃ layer, quite different results have been reported^{5,170-173} and the band diagrams proposed for the hybrid perovskite solar cells have been highly controversial.^{4,170,171,174-177} It is generally assumed that the operation of CH₃NH₃PbI₃ solar cells occurs by the formation of a *p-i-n* type structure.^{5,173-178} Indeed, when EBIC measurements were implemented for CH₃NH₃PbI_{3-x}Cl_x solar cells having the thick absorber layers (1.5 μm), the presence of two intense electric-field regions was confirmed near the TiO₂/CH₃NH₃PbI_{3-x}Cl_x and CH₃NH₃PbI_{3-x}Cl_x/HTL interfaces.⁴ Nevertheless, other studies based on Kelvin force microscopy reported that the electric field concentrates at the TiO₂/CH₃NH₃PbI₃ (or CH₃NH₃PbI_{3-x}Cl_x) interface^{170,172} and several studies concluded^{115,170-172} that the hybrid perovskite solar cell operates as a simple *p-n* junction device.

This controversy can be interpreted by the carrier type of CH₃NH₃PbI₃ layers. To date, *n*-type conductivities of CH₃NH₃PbI₃ layers have been confirmed by Seebeck¹⁷⁹ and Hall¹⁸⁰ measurements. In solution-based processing of CH₃NH₃PbI₃, however, the carrier type changes from *p*-type to *n*-type with increasing PbI₂/CH₃NH₃I precursor ratio.¹⁸⁰ Thus, CH₃NH₃PbI₃ layers show the *n*-type carrier conduction when the PbI₂-rich phase is formed, although CH₃NH₃PbI₃ single crystals exhibit the *p*-type character with a low N_p value of 9×10^9 cm⁻³.¹⁸¹ The earlier UPS measurement further confirmed that, when a CH₃NH₃PbI₃ layer is fabricated by a standard condition (PbI₂/CH₃NH₃I = 1), E_F shifts toward CBM with an electron concentration of 3×10^{17} cm⁻³.¹⁸⁰

Our EQE analyses in Fig. 17 strongly support the formation of the *n*-type CH₃NH₃PbI₃. In particular, when the CH₃NH₃PbI₃ layer shows *n*-type conductivity, the electric field is expected to concentrate at the CH₃NH₃PbI₃(*n*)/HTL(*p*) interface with a weak electric field at the TiO₂(*n*)/CH₃NH₃PbI₃(*n*) interface, as schematically shown in

Fig. 21(d). Thus, the relatively strong front-carrier recombination near the TiO_2 interface [i.e., recombination pass C in Fig. 21(d)] could be explained by the weaker electric field in this region. In contrast, the recombination in the solar-cell bottom region is suppressed almost completely most likely due to the presence of the strong field near the HTL. Based on the above result, we propose that, in $\text{CH}_3\text{NH}_3\text{PbI}_3$ solar cells, the electric-field-assisted carrier collection ($L_C \sim W$) occurs by the formation of a $p-n^- - n$ type structure (or $n-n^- - p$ from the light illumination side).

This situation changes significantly when an HTL is not present. In this case, the flat-band formation is expected to occur by the elimination of the strong electric field in the bottom region. In this device, the photocarrier collection could be limited by the carrier diffusion, similar to the case of the CZTSe solar cell in Fig. 21(b), and the intensified recombination in the rear interface region lowers the EQE response in the longer λ region, as pointed out previously.¹¹⁴ In fact, the previous EBIC study confirmed that the strong electric field present at the $\text{CH}_3\text{NH}_3\text{PbI}_{3-x}\text{Cl}_x/\text{HTL}$ interface disappears completely when the HTL is removed from the device.⁴ Thus, lower V_{oc} observed in $\text{CH}_3\text{NH}_3\text{PbI}_3$ solar cells with no HTL^{112-114,182} can be interpreted by the smaller built-in potential. In contrast, the presence of the HTL does not affect the electric-field distribution within the $\text{CH}_3\text{NH}_3\text{PbI}_3$ when the $p-n$ junction is formed.¹⁷² The above evidences lead us to conclude that the strong electric field is generated at the $\text{CH}_3\text{NH}_3\text{PbI}_3/\text{HTL}$ for the n -type $\text{CH}_3\text{NH}_3\text{PbI}_3$, whereas the electric field concentrates at the $\text{CH}_3\text{NH}_3\text{PbI}_3/\text{TiO}_2$ for the p -type $\text{CH}_3\text{NH}_3\text{PbI}_3$. Nevertheless, the drastic reduction of the EQE response by the removal of an HTL has commonly been observed in $\text{CH}_3\text{NH}_3\text{PbI}_3$ solar cells.¹¹²⁻¹¹⁵ Accordingly, we believe that $\text{CH}_3\text{NH}_3\text{PbI}_3$ layers incorporated into high-efficiency hybrid perovskite solar cells basically have n -type character.

Earlier DFT studies further revealed that mid-gap states are not created by the vacancy/interstitial-type defects in $\text{CH}_3\text{NH}_3\text{PbI}_3$,¹⁸³⁻¹⁸⁵ although the formation of complex defects is still possible.¹⁸⁶ Moreover, in the grain boundary region of $\text{CH}_3\text{NH}_3\text{PbI}_3$, the PbI_2 -rich phase having larger E_g is formed, suppressing the carrier recombination in the grain boundary region effectively.¹⁸⁷ The efficient carrier extraction from $\text{CH}_3\text{NH}_3\text{PbI}_3$ grain boundary regions has also been reported by SPM¹⁸⁸ and EBIC.¹⁸⁹ In $\text{CH}_3\text{NH}_3\text{PbI}_3$ solar cells, therefore, the carrier recombination is expected to occur predominantly in the front and rear interface regions with limited recombination within the bulk region. However, it has recently been reported that the grain size of $\text{CH}_3\text{NH}_3\text{PbI}_3$ affects V_{oc} .¹⁹⁰ In this point of view, $\text{CH}_3\text{NH}_3\text{PbI}_3$ solar cells show a feature of polycrystalline solar cells and are similar to CIGSe, CZT(S)Se and

CdTe solar cells.

The EQE analyses performed for CZT(S)Se, CdTe and $\text{CH}_3\text{NH}_3\text{PbI}_3$ solar cells in this study consistently suggest that the intense carrier recombination occurs when the flat band is formed. This is in sharp contrast to crystalline Si-based solar cells, in which a quite long carrier life time (~ 1 ms)¹⁹¹ results in a quite long L_D (~ 2000 μm) of photo-generated carriers. Accordingly, in thin-film solar cells with limited carrier life time and L_D , the electric-field-assisted carrier collection is of paramount importance to realize high conversion efficiencies.

C. Effect of L_C on J_{sc}

Figure 22 shows the variation of J_{sc} with L_C for various solar cells calculated from the e-ARC method. For all the solar cells, we assumed an identical solar cell structure consisting of the MgF_2 (130 nm)/ $\text{ZnO}:\text{Al}$ (360 nm)/ ZnO (50 nm)/ CdS (45 nm)/absorber (2.0 μm)/ Mo , except for CdTe and $\text{CH}_3\text{NH}_3\text{PbI}_3$ solar cells. For the CdTe and $\text{CH}_3\text{NH}_3\text{PbI}_3$ solar cells, the structures of Fig. 15 (CdTe) and Fig. 17(a) ($\text{CH}_3\text{NH}_3\text{PbI}_3$) were adopted, but we performed the calculation using an identical absorber thickness of 2.0 μm to compare the intrinsic properties of the absorber layers. In the calculation of the $\text{CH}_3\text{NH}_3\text{PbI}_3$ solar cell, the thickness of the front dead layer is assumed to be zero. For the dielectric functions of the absorbers, the optical data of Fig. 4 were employed, although E_g is increased slightly for the CZTSe ($E_g = 1.0$ eV) and the CZTS ($E_g = 1.45$ eV) based on the results of Fig. 14.

In Fig. 22, J_{sc} is higher in the solar cell with a low- E_g absorber and J_{sc} increases rapidly with increasing L_C . The variations of J_{sc} with L_C are essentially similar in all the solar cells, and J_{sc} tends to saturate at $L_C > 1.0$ μm . Nevertheless, the J_{sc} values of CdTe and $\text{CH}_3\text{NH}_3\text{PbI}_3$ solar cells show almost complete saturation at $L_C > 1.0$ μm . This trend originates from the sharp absorption features of these absorbers, as confirmed in Fig. 4. Consequently, in CdTe and $\text{CH}_3\text{NH}_3\text{PbI}_3$ solar cells, J_{sc} is not influenced by the recombination as long as the condition of $L_C > 1.0$ μm is satisfied. Thus, the dispersion of the α spectrum is quite important in interpreting the carrier generation/recombination. For solar cells, it is preferable if a light absorber has high α values near E_g with a low Urbach energy (sharp absorption onset). The CdTe and $\text{CH}_3\text{NH}_3\text{PbI}_3$ semiconductors appear to fulfill these conditions relatively well.

VI. CONCLUSION

We developed a general EQE analysis method that allows the quantitative description of the optical and carrier recombination losses within thin-film solar cells. In the developed method, the light scattering caused by submicron textures is expressed by imposing anti-reflection condition in the calculation of the optical admittance method and the carrier recombination is further modeled based on exponential-decaying carrier extraction from the absorber interface using L_C as a sole parameter. Although our EQE analysis method is quite simple, it is sufficient to determine optical and recombination losses quantitatively. In particular, if the optical constants and thickness of each layer are known, the EQE spectrum can be calculated quite easily without considering geometrical structures.

The developed method was applied to variety of solar cell devices fabricated by coevaporation, sputtering, closed-space sublimation and solution-based processes, and provides almost perfect fitting to numerous EQE spectra reported earlier. From our EQE analyses, the L_C values in CZTSe, CZTS, CZTSSe, CdTe and $\text{CH}_3\text{NH}_3\text{PbI}_3$ solar cells were estimated. We found that J_{sc} in the CZTSe and CZTSSe solar cells is limited severely by low L_C values, originating from the intense recombination in the absorber bottom region. In contrast, CdTe and $\text{CH}_3\text{NH}_3\text{PbI}_3$ solar cells show small recombination losses. Finally, we emphasize that the developed method allows the fast and easy analysis of EQE spectra obtained from various thin-film solar cells without the requirement of intensive computer modeling for surface and interface structures. Accordingly, the EQE analysis technique developed in this study provides an ideal method for determining various limiting factors in thin-film photovoltaic devices.

Reference list

- ¹A. Luque and S. Hegedus, *Handbook of Photovoltaic Science and Engineering* (Wiley, West Sussex, UK, 2011).
- ²S. A. Galloway, P. R. Edwards and K. Durose, *Sol. Energy Mater. Sol. Cells* **57**, 61 (1999).
- ³G. Brown, V. Faifer, A. Pudov, S. Anikeev, E. Bykov, M. Contreras and J. Wu, *Appl. Phys. Lett.* **96**, 022104 (2010).
- ⁴E. Edri, S. Kirmayer, S. Mukhopadhyay, K. Gartsman, G. Hodes and D. Cahen, *Nat. Commun.* **5**, 3461 (2014).
- ⁵E. Edri, S. Kirmayer, A. Henning, S. Mukhopadhyay, K. Gartsman, Y. Rosenwaks, G. Hodes and D. Cahen, *Nano Lett.* **14**, 1000 (2014).
- ⁶O. Gunawan, T. K. Todorov and D. B. Mitzi, *Appl. Phys. Lett.* **97**, 233506 (2010).
- ⁷S. D. Stranks, G. E. Eperon, G. Grancini, C. Menelaou, M. J. P. Alcocer, T. Leijtens, L. M. Herz, A. Petrozza and H. J. Snaith, *Science* **342**, 341 (2013).
- ⁸G. Xing, N. Mathews, S. Sun, S. S. Lim, Y. M. Lam, M. Grätzel, S. Mhaisalkar and T. C. Sum, *Science* **342**, 344 (2013).
- ⁹P. R. Edwards, S. A. Galloway and K. Durose, *Thin Solid Films* **361–362**, 364 (2000).
- ¹⁰A. Kanevce, D. H. Levi and D. Kuciauskas, *Prog. Photovoltaics* **22**, 1138 (2014).
- ¹¹W. K. Metzger, I. L. Repins and M. A. Contreras, *Appl. Phys. Lett.* **93**, 022110 (2008).
- ¹²M. Lavagna, J. P. Pique and Y. Marfaing, *Solid-State Electronics* **20**, 235 (1977).
- ¹³X. X. Liu and J. R. Sites, *J. Appy. Phys.* **75**, 577 (1994).
- ¹⁴S. S. Hegedus and W. N. Shafarman, *Prog. Photovoltaics* **12**, 155 (2004).
- ¹⁵T. Gokmen, O. Gunawan and D. B. Mitzi, *J. Appl. Phys.* **114**, 114511 (2013).
- ¹⁶I. L. Repins, H. Moutinho, S. G. Choi, A. Kanevce, D. Kuciauskas, P. Dippo, C. L. Beall, J. Carapella, C. DeHart, B. Huang and S. H. Wei, *J. Appl. Phys.* **114**, 084507 (2013).
- ¹⁷W. Wang, M. T. Winkler, O. Gunawan, T. Gokmen, T. K. Todorov, Y. Zhu and D. B. Mitzi, *Adv. Energy Mater.* **4**, 1301465 (2014).
- ¹⁸C. J. Hages, N. J. Carter and R. Agrawal, *J. Appl. Phys.* **119**, 014505 (2016).
- ¹⁹T. Hara, T. Maekawa, S. Minoura, Y. Sago, S. Niki and H. Fujiwara, *Phys. Rev. Applied* **2**, 034012 (2014).
- ²⁰S. C. Baker-Finch and K. R. McIntosh, *Prog. Photovoltaics* **19**, 406 (2011).
- ²¹M. Agrawal and M. Frei, *Prog. Photovoltaics* **20**, 442 (2012).
- ²²M. Zeman, O. Isabella, S. Solntsev and K. Jäger, *Sol. Energy Mater. Sol. Cells* **119**, 94 (2013).

- ²³Y. S. Lee, T. Gershon, O. Gunawan, T. K. Todorov, T. Gokmen, Y. Virgus and S. Guha, *Adv. Energy Mater.* **5**, 1401372 (2015).
- ²⁴S. Bag, O. Gunawan, T. Gokmen, Y. Zhu, T. K. Todorov and D. B. Mitzi, *Energy Environ. Sci.* **5**, 7060 (2012).
- ²⁵J.-O. Jeon, K. D. Lee, L. S. Oh, S.-W. Seo, D.-K. Lee, H. Kim, J.-H. Jeong, M. J. Ko, B. Kim, H. J. Son and J. Y. Kim, *ChemSusChem* **7**, 1073 (2014).
- ²⁶A. Redinger, M. Mousel, M. H. Wolter, N. Valle and S. Siebentritt, *Thin Solid Films* **535**, 291 (2013).
- ²⁷A. Redinger, M. Mousel, R. Djemour, L. Gütay, N. Valle and S. Siebentritt, *Prog. Photovoltaics* **22**, 51 (2014).
- ²⁸T. K. Todorov and K. B. Reuter and D. B. Mitzi, *Adv. Mater.* **22**, E156 (2010).
- ²⁹I. Repins, C. Beall, N. Vora, C. DeHart, D. Kuciauskas, P. Dippo, B. To, J. Mann, W.-C. Hsu, A. Goodrich and R. Noufi, *Sol. Energy Mater. Sol. Cells* **101**, 154 (2012).
- ³⁰S. Oueslati, G. Brammertz, M. Buffière, H. ElAnzeery, O. Touayar, C. Köble, J. Bekaert, M. Meuris and J. Poortmans, *Thin Solid Films* **582**, 224 (2015).
- ³¹B. Shin, O. Gunawan, Y. Zhu, N. A. Bojarczuk, S. J. Chey and S. Guha, *Prog. Photovoltaics* **21**, 72 (2013).
- ³²T. Fukano, S. Tajima and T. Ito, *Appl. Phys. Express* **6**, 062301 (2013).
- ³³M. G. Gang, K. V. Gurav, S. W. Shin, C. W. Hong, J. H. Min, M. P. Suryawanshi, S. A. Vanalakar, D. S. Lee and J. H. Kim, *Phys. Status Solidi C* **12**, 713 (2015).
- ³⁴T. P. Dhakal, C.-Y. Peng, R. R. Tobias, R. Dasharathy and C. R. Westgate, *Solar Energy* **100**, 23 (2014).
- ³⁵H. Cui, X. Liu, F. Liu, X. Hao, N. Song and C. Yan, *Appl. Phys. Lett.* **104**, 041115 (2014).
- ³⁶A. Ennaoui, M. L.-Steiner, A. Weber, D. Abou-Ras, I. Kötschau, H.-W. Schock, R. Schurr, A. Hölzing, S. Jost, R. Hock, T. Voß, J. Schulze and A. Kirbs, *Thin Solid Films* **517**, 2511 (2009).
- ³⁷S. Ahmed, K. B. Reuter, O. Gunawan, L. Guo, L. T. Romankiw and H. Deligianni, *Adv. Energy Mater.* **2**, 253 (2012).
- ³⁸J. J. Scragg, T. Ericson, X. Fontané, V. Izquierdo-Roca, A. Pérez-Rodríguez, T. Kubart, M. Edoff and C. Platzer-Björkman, *Prog. Photovoltaics* **22**, 10 (2014).
- ³⁹F. Zhou, F. Zeng, X. Liu, F. Liu, N. Song, C. Yan, A. Pu, J. Park, K. Sun and X. Hao, *ACS Appl. Mater. Interfaces* **7**, 22868 (2015).
- ⁴⁰J. Kim, H. Hiroi, T. K. Todorov, O. Gunawan, M. Kuwahara, T. Gokmen, D. Nair, M. Hopstaken, B. Shin, Y. S. Lee, W. Wang, H. Sugimoto and D. B. Mitzi, *Adv. Mater.* **26**, 7427 (2014).

- ⁴¹C. J. Hages, S. Levchenko, C. K. Miskin, J. H. Alsmeier, D. Abou-Ras, R. G. Wilks, M. Bär, T. Unold and R. Agrawal, *Prog. Photovoltaics* **23**, 376 (2015).
- ⁴²G. Larramona, S. Bourdais, A. Jacob, C. Choné, T. Muto, Y. Cuccaro, B. Delatouche, C. Moisan, D. Péré and G. Dennler, *J. Phys. Chem. Lett.* **5**, 3763 (2014).
- ⁴³H. Xie, M. Dimitrievska, X. Fontané, Y. Sánchez, S. L.-Marino, V. Izquierdo-Roca, V. Bermúdez, A. Pérez-Rodríguez and E. Saucedo, *Sol. Energy Mater. Sol. Cells* **140**, 289 (2015).
- ⁴⁴Q. Guo, G. M. Ford, W.-C. Yang, B. C. Walker, E. A. Stach, H. W. Hillhouse and R. Agrawal, *J. Am. Chem. Soc.* **132**, 17384 (2010).
- ⁴⁵H. Xin, J. K. Katahara, I. L. Braly and H. W. Hillhouse, *Adv. Energy Mater.* **4**, 1301823 (2014).
- ⁴⁶C. K. Miskin, W.-C. Yang, C. J. Hages, N. J. Carter, C. S. Joglekar, E. A. Stach and R. Agrawal, *Prog. Photovoltaics* **23**, 654 (2015).
- ⁴⁷G. Larramona, S. Levchenko, S. Bourdais, A. Jacob, C. Choné, B. Delatouche, C. Moisan, J. Just, T. Unold and G. Dennler, *Adv. Energy Mater.* **5**, 1501404 (2015).
- ⁴⁸T. Aramoto, S. Kumazawa, H. Higuchi, T. Arita, S. Shibutani, T. Nishio, J. Nakajima, M. Tsuji, A. Hanafusa, T. Hibino, K. Omura, H. Ohyama and M. Murozono, *Jpn. J. Appl. Phys.* **36**, 6304 (1997).
- ⁴⁹J. H. Heo, D. H. Song, H. J. Han, S. Y. Kim, J. H. Kim, D. Kim, H. W. Shin, T. K. Ahn, C. Wolf, T.-W. Lee and S. H. Im, *Adv. Mater.* **27**, 3424 (2015).
- ⁵⁰J. Shi, J. Dong, S. Lv, Y. Xu, L. Zhu, J. Xiao, X. Xu, H. Wu, D. Li, Y. Luo and Q. Meng, *Appl. Phys. Lett.* **104**, 063901 (2014).
- ⁵¹H. Tampo, K. Makita, H. Komaki, A. Yamada, S. Furue, S. Isizuka, H. Shibata, K. Matsubara and S. Niki, *Thin Solid Films* **551**, 27 (2014).
- ⁵²Y. Hashimoto, N. Kohara, T. Negami, N. Nishitani and T. Wada, *Sol. Energy Mater. Sol. Cells* **50**, 71 (1998).
- ⁵³G. Brammertz, M. Buffière, S. Oueslati, H. ElAnzeery, K. B. Messaoud, S. Sahayaraj, C. Köble, M. Meuris and J. Poortmans, *Appl. Phys. Lett.* **103**, 163904 (2013).
- ⁵⁴B. Shin, Y. Zhu, N. A. Bojarczuk, S. J. Chey and S. Guha, *Appl. Phys. Lett.* **101**, 053903 (2012).
- ⁵⁵B. Shin, N. A. Bojarczuk and S. Guha, *Appl. Phys. Lett.* **102**, 091907 (2013).
- ⁵⁶H. A. Macleod, *Thin-Film Optical Filters* (CRC Press, NY, 2010).
- ⁵⁷J. A. Berning and P. H. Berning, *J. Opt. Soc. Am.* **50**, 813 (1960).
- ⁵⁸A. Y. Darkwi, W. K. Loke and K. Ibrahim, *Sol. Energy Mater. Sol. Cells* **60**, 1 (2000).
- ⁵⁹H. Fujiwara, *Spectroscopic Ellipsometry: Principles and Applications* (Wiley, West Sussex, UK, 2007).

- ⁶⁰D. E. Aspnes, *Thin Solid Films* **89**, 249 (1982).
- ⁶¹Y. Hirate, H. Tampo, S. Minoura, H. Kadowaki, A. Nakane, K. M. Kim, H. Shibata, S. Niki and H. Fujiwara, *J. Appl. Phys.* **117**, 015702 (2015).
- ⁶²J. Chen, J. Li, D. Sainju, K. D. Wells, N. J. Podraza and R. W. Collins, *Proceedings of IEEE 4th World Conference on Photovoltaic Energy Conversion* (IEEE, New York, 2006), p. 711.
- ⁶³M. Richter, C. Schubbert, P. Eraerds, I. Riedel, J. Keller, J. Parisi, T. Dalibor and A. Avellan-Hampe, *Thin Solid Films* **535**, 331 (2013).
- ⁶⁴R. Klenk, H. Schock and W. Bloss, *Proceeding of the 12th Euro. Conf. Photovoltaic Solar Energy Conversion* (EUPVSEC, Amsterdam, 1994), p. 1588.
- ⁶⁵M. Shirayama, H. Kadowaki, T. Miyadera, T. Sugita, M. Tamakoshi, M. Kato, T. Fujiseki, D. Murata, S. Hara, T. N. Murakami, S. Fujimoto, M. Chikamatsu and H. Fujiwara, *Phys. Rev. Applied* **5**, 014012 (2016).
- ⁶⁶S. Minoura, K. Kodera, T. Maekawa, K. Miyazaki, S. Niki and H. Fujiwara, *J. Appl. Phys.* **113**, 063505 (2013).
- ⁶⁷S. Minoura, T. Maekawa, K. Kodera, A. Nakane, S. Niki and H. Fujiwara, *J. Appl. Phys.* **117**, 195703 (2015).
- ⁶⁸J. Li, H. Du, J. Yarbrough, A. Norman, K. Jones, G. Teeter, F. L. Terry Jr. and D. Levi, *Opt. Express* **20**, A327 (2012).
- ⁶⁹S. Adachi, *Optical Constants of Crystalline and Amorphous Semiconductors* (Kluwer Academic Publishers, Norwell, 1999).
- ⁷⁰P. Koirala, J. Li, H. P. Yoon, P. Aryal, S. Marsillac, A. A. Rockett, N. J. Podraza and R. W. Collins, *Prog. Photovoltaics* DOI: 10.1002/pip.2759 (2016).
- ⁷¹J. Paier, R. Asahi, A. Nagoya and G. Kresse, *Phys. Rev. B* **79**, 115126 (2009).
- ⁷²C. Persson, *J. Appl. Phys.* **107**, 053710 (2010).
- ⁷³J. E. Jaffe and A. Zunger, *Phys. Rev. B* **29**, 1882 (1984).
- ⁷⁴J. E. Jaffe and A. Zunger, *Phys. Rev. B* **28**, 5822 (1983).
- ⁷⁵M. P. Marder, *Condensed Matter Physics* (Wiley, Hoboken, 2010).
- ⁷⁶S. Chen, A. Walsh, J.-H. Yang, X. G. Gong, L. Sun, P.-X. Yang, J.-H. Chu and S.-H. Wei, *Phys. Rev. B* **83**, 125201 (2011).
- ⁷⁷P. G. Snyder, J. A. Woollam, S. A. Alterovitz and B. Johs, *J. Appl. Phys.* **68**, 5925 (1990).
- ⁷⁸J. He, L. Sun, S. Chen, Y. Chen, P. Yang and J. Chu, *J. Alloys Compd.* **511**, 129 (2012).
- ⁷⁹F. Gao, S. Yamazoe, T. Maeda, K. Nakanishi and T. Wada, *Jpn. J. Appl. Phys.* **51**, 10NC29 (2012).

- ⁸⁰H. Fujiwara and M. Kondo, Phys. Rev. B **71**, 075109 (2005).
- ⁸¹K. Sago, H. Kuramochi, H. Iigusa, K. Utsumi and H. Fujiwara, J. Appl. Phys. **115**, 133505 (2014).
- ⁸²B. E. Sernelius, K.-F. Berggren, Z.-C. Jin, I. Hamberg and C. G. Granqvist, Phys. Rev. B **37**, 10244 (1988).
- ⁸³A. Walsh, J. L. F. D. Silva and S.-H. Wei, Phys. Rev. B **78**, 075211 (2008).
- ⁸⁴M. Feneberg, J. Nixdorf, C. Lidig and R. Goldhahn, Phys. Rev. B **93**, 045203 (2016).
- ⁸⁵A. R. Beal and H. P. Hughes, J. Phys. C **12**, 881 (1979).
- ⁸⁶S. Adachi, *The Handbook on Optical Constants of Metals* (World Scientific, Singapore, 2012).
- ⁸⁷J. Chen, J. Li, C. Thornberry, M. N. Sestak, R. W. Collins, J. D. Walker, S. Marsillac, A. R. Aquino and A. Rockett, *Proceeding of the 34th IEEE PVSC* (IEEE, New York, 2009), p. 1748.
- ⁸⁸E. D. Palik, *Handbook of Optical Constants of Solids* (Academic Press, Orlando, 1985).
- ⁸⁹S. Chen, L.-W. Wang, A. Walsh, X. G. Gong and S.-H. Wei, Appl. Phys. Lett. **101**, 223901 (2012).
- ⁹⁰C. S. Ferekides, D. Marinskiy, V. Viswanathan, B. Tetali, V. Palekis, P. Selvaraj and D. L. Morel, Thin Solid Films **361–362**, 520 (2000).
- ⁹¹N. Romeo, A. Bosio, V. Canevari and A. Podestà, Solar Energy **77**, 795 (2004).
- ⁹²B. E. McCandless, L. V. Moulton and R.W. Birkmire, Prog. Photovoltaics **5**, 249 (1997).
- ⁹³X. Wu, Solar Energy **77**, 803 (2004).
- ⁹⁴B. E. McCandless and K. D. Dobson, Solar Energy **77**, 839 (2004).
- ⁹⁵M. A. Green, K. Emery, Y. Hishikawa, W. Warta and E. D. Dunlop, Prog. Photovoltaics **23**, 805 (2015).
- ⁹⁶J. Sinkkonen, J. Ruokolainen, P. Uotila and A. Hovinen, Appl. Phys. Lett. **66**, 206 (1995).
- ⁹⁷D. Desai, S. Hegedus, B. McCandless, R. Birkmire, K. Dobson and D. Ryan, *Proceedings of IEEE 4th World Conference on Photovoltaic Energy Conversion* (IEEE, New York, 2006), p. 368.
- ⁹⁸L. Kosyachenko and T. Toyama, Sol. Energy Mater. Sol. Cells **120**, 512 (2014).
- ⁹⁹L. A. Kosyachenko, E. V. Grushko and X. Mathew, Sol. Energy Mater. Sol. Cells **96**, 231 (2012).
- ¹⁰⁰H. A. Mohamed, J. Appl. Phys. **113**, 093105 (2013).

- ¹⁰¹L. Tarricone, N. Romeo, G. Sberveglieri and S. Mora, *Sol. Energy Mater.* **7**, 343 (1982).
- ¹⁰²J. Toušek, D. Kindl, J. Toušková and S. Dolhov, *J. Appl. Phys.* **89**, 460 (2001).
- ¹⁰³D. L. Bätzner, M. E. Öszan, D. Bonnet, K. Bücher, *Thin Solid Films* **361–362**, 288 (2000).
- ¹⁰⁴A. Kojima, K. Teshima, Y. Shirai and T. Miyasaka, *J. Am. Chem. Soc.* **131**, 6050 (2009).
- ¹⁰⁵M. M. Lee, J. Teuscher, T. Miyasaka, T. N. Murakami and H. J. Snaith, *Science* **338**, 643 (2012).
- ¹⁰⁶P. Gao, M. Grätzel and M. K. Nazeeruddin, *Energy Environ. Sci.* **7**, 2448 (2014).
- ¹⁰⁷H. S. Jung and N.-G. Park, *Small* **11**, 10 (2015).
- ¹⁰⁸J.-H. Kwon, S.-I. Shin, J. Choi, M.-H. Chung, T.-Y. Oh, K.-H. Kim, M. J. Cho, K. N. Kim, D. H. Choi and B.-K. Ju, *Organic Electronics* **10**, 729 (2009).
- ¹⁰⁹J. M. Ball, S. D. Stranks, M. T. Hörantner, S. Hüttner, W. Zhang, E. J. W. Crossland, I. Ramirez, M. Riede, M. B. Johnston, R. H. Friend and H. J. Snaith, *Energy Environ. Sci.* **8**, 602 (2015).
- ¹¹⁰P. Docampo, S. Guldin, M. Stefič, P. Tiwana, M. C. Orilall, S. Hüttner, H. Sai, U. Wiesner, U. Steiner and H. J. Snaith, *Adv. Funct. Mater.* **20**, 1787 (2010).
- ¹¹¹J. Lin, Y.-U. Heo, A. Nattestad, Z. Sun, L. Wang, J. H. Kim and S. X. Dou, *Sci. Rep.* **4**, 5769 (2014).
- ¹¹²L. Etgar, P. Gao, Z. Xue, Q. Peng, A. K. Chandiran, B. Liu, M. K. Nazeeruddin and M. Grätzel, *J. Am. Chem. Soc.* **134**, 17396 (2012).
- ¹¹³H. Zhou, Y. Shi, Q. Dong, H. Zhang, Y. Xing, K. Wang, Y. Du and T. Ma, *J. Phys. Chem. Lett.* **5**, 3241 (2014).
- ¹¹⁴W. Tress, N. Marinova, O. Inganäs, M. K. Nazeeruddin, S. M. Zakeeruddin and M. Graetzel, *Adv. Energy Mater.* **5**, 1400812 (2014).
- ¹¹⁵A. R. B. M. Yuoff and M. K. Nazeeruddin, *J. Phys. Chem. Lett.* **7**, 851 (2016).
- ¹¹⁶M. T. Winkler, W. Wang, O. Gunawan, H. J. Hovel, T. K. Todorov and D. B. Mitzi, *Energy Environ. Sci.* **7**, 1029 (2014).
- ¹¹⁷J. W. Bowers, H. M. Upadhyaya, S. Calnan, R. Hashimoto, T. Nakada and A. N. Tiwari, *Prog. Photovoltaic* **17**, 265 (2009).
- ¹¹⁸D. S. Bhachu, M. R. Waugh, K. Zeissler, W. R. Branford and I. P. Parkin, *Chem. Eur. J.* **17**, 11613 (2011).
- ¹¹⁹T. Koida, H. Fujiwara and M. Kondo, *Jpn. J. Appl. Phys.* **46**, L685 (2007).
- ¹²⁰T. Koida, H. Fujiwara and M. Kondo, *Sol. Energy Mater. Sol. Cells* **93**, 851 (2009).

- ¹²¹T. Koida, M. Kondo, K. Tsutsumi, A. Sakaguchi, M. Suzuki and H. Fujiwara, *J. Appl. Phys.* **107**, 033514 (2010).
- ¹²²B. A. Korevaar, A. Halverson, J. Cao, J. Choi, C. Collazo-Davila and W. Huber, *Thin Solid Films* **535**, 229 (2013).
- ¹²³K. Orgassa, H. W. Schock and J. H. Werner, *Thin Solid Films* **431-432**, 387 (2003).
- ¹²⁴J. Malmström, S. Schleussner and L. Stolt, *Appl. Phys. Lett.* **85**, 2634 (2004).
- ¹²⁵Z. J. Li-Kao, N. Naghavi, F. Erfurth, J. F. Guillemoles, I. Gérard, A. Etcheberry, J. L. Pelouard, S. Collin, G. Voorwinden and D. Lincot, *Prog. Photovoltaic* **20**, 582 (2012).
- ¹²⁶U. Rau and H. W. Schock, *Appl. Phys. A* **69**, 131 (1999).
- ¹²⁷O. Lundberg, M. Edoff and L. Stolt, *Thin Solid Films* **480-481**, 520 (2005).
- ¹²⁸M. Gloeckler and J. R. Sites, *Thin Solid Films* **480-481**, 241 (2005).
- ¹²⁹A. Chirilă, S. Buecheler, F. Pianezzi, P. Bloesch, C. Gretener, A. R. Uhl, C. Fella, L. Kranz, J. Perrenoud, S. Seyrling, R. Verma, S. Nishiwaki, Y. E. Romanyuk, G. Bilger and A. N. Tiwari, *Nat. Mater.* **10**, 857 (2011).
- ¹³⁰J. Pettersson, T. Törndahl, C. Platzer-Björkman, A. Hultqvist and M. Edoff, *IEEE J. Photovoltaics* **3**, 1376 (2013).
- ¹³¹R. Haight, A. Barkhouse, O. Gunawan, B. Shin, M. Copel, M. Hopstaken and D. B. Mitzi, *Appl. Phys. Lett.* **98**, 253502 (2011).
- ¹³²T. Kato, H. Hiroi, N. Sakai and H. Sugimoto, *Proceeding of the 28th Euro. Photovoltaic Solar Energy Conf. (EUPVSEC, Paris, 2013)*, p. 2125.
- ¹³³M. Buffière, G. Brammertz, S. Oueslati, H. E. Anzeery, J. Bekaert, K. B. Messaoud, C. Köble, S. Khelifi, M. Meuris and J. Poortmans, *J. Phys. D* **47**, 175101 (2014).
- ¹³⁴A. Kanevce, I. Repins and S.-H. Wei, *Sol. Energy Mater. Sol. Cells* **133**, 119 (2015).
- ¹³⁵C. R. Corwine, A. O. Pudov, M. Gloeckler, S. H. Demtsu and J. R. Sites, *Sol. Energy Mater. Sol. Cells* **82**, 481 (2004).
- ¹³⁶S. H. Demtsu and J. R. Sites, *Thin Solid Films* **510**, 320 (2006).
- ¹³⁷J. Sites and J. Pan, *Thin Solid Films* **515**, 6099 (2007).
- ¹³⁸M. Bär, S. Nishiwaki, L. Weinhardt, S. Pookpanratana, W. N. Shafarman and C. Heske, *Appl. Phys. Lett.* **93**, 042110 (2008).
- ¹³⁹A. M. Gabor, J. R. Tuttle, D. S. Albin, M. A. Contreras, R. Noufi and A. M. Hermann, *Appl. Phys. Lett.* **65**, 198 (1994).
- ¹⁴⁰A. M. Gabor, J. R. Tuttle, M. H. Bode, A. Franz, A. L. Tennant, M. A. Contreras, R. Noufi, D. G. Jensen and A. M. Hermann, *Sol. Energy Mater. Sol. Cells* **41-42**, 247 (1996).

- ¹⁴¹M. A. Contreras, J. Tuttle, A. Gabor, A. Tennant, K. Ramanathan, S. Asher, A. Franz, J. Keane, L. Wang and R. Noufi, *Sol. Energy Mater. Sol. Cells* **41-42**, 231 (1996).
- ¹⁴²P. Jackson, D. Hariskos, R. Wuerz, O. Kiowski, A. Bauer, T. M. Friedlmeier and M. Powalla, *Phys. Status Solidi RRL* **9**, 28 (2015).
- ¹⁴³S. Wei, S. B. Zhang and A. Zunger, *Appl. Phys. Lett.* **72**, 3199 (1998).
- ¹⁴⁴M. Turcu and U. Rau, *Thin Solid Films* **431-432**, 158 (2003).
- ¹⁴⁵N. Terada, R. T. Widodo, K. Itoh, S. H. Kong, H. Kashiwabara, T. Okuda, K. Obara, S. Niki, K. Sakurai, A. Yamada and S. Ishizuka, *Thin Solid Films* **480-481**, 183 (2005).
- ¹⁴⁶T. Dullweber, O. Lundberg, J. Malmström, M. Bodegård, L. Stolt, U. Rau, H. W. Schock and J. H. Werner, *Thin Solid Films* **387**, 11 (2001).
- ¹⁴⁷I. L. Repins, M. J. Romero, J. V. Li, S.-H. Wei, D. Kuciauskas, C.-S. Jiang, C. Beall, C. DeHart, J. Mann, W.-C. Hsu, G. Teeter, A. Goodrich and R. Noufi, *IEEE J. Photovoltaics* **3**, 439 (2013).
- ¹⁴⁸M. Gloeckler and J. R. Sites, *J. Appl. Phys.* **98**, 103703 (2005).
- ¹⁴⁹K. Wang, B. Shin, K. B. Reuter, T. Todorov, D. B. Mitzi and S. Guha, *Appl. Phys. Lett.* **98**, 051912 (2011).
- ¹⁵⁰J. B. Li, V. Chawla and B. M. Clemens, *Adv. Mater.* **24**, 720 (2012).
- ¹⁵¹J. E. Moore, C. J. Hages, R. Agrawal, M. S. Lundstrom, and J. L. Gray, *Appl. Phys. Lett.* **109**, 021102 (2016).
- ¹⁵²C. G. Van de Walle and J. Neugebauer, *Nature* **423**, 626 (2003).
- ¹⁵³K. D. Dobson, I. Visoly-Fisher, G. Hodes and D. Cahen, *Sol. Energy Mater. Sol. Cells* **62**, 295 (2000).
- ¹⁵⁴D. L. Bätzner, A. Romeo, M. Terheggen, M. Döbeli, H. Zogg and A. N. Tiwari, *Thin Solid Films* **451-452**, 536 (2004).
- ¹⁵⁵L. A. Kosyachenko, A. I. Savchuk and E. V. Grushko, *Thin Solid Films* **517**, 2386 (2009).
- ¹⁵⁶J. N. Duenow, J. M. Burst, D. S. Albin, D. Kuciauskas, S. W. Johnston, R. C. Reedy and W. K. Metzger, *Appl. Phys. Lett.* **105**, 053903 (2014).
- ¹⁵⁷N. Amin, K. Sopian and M. Konagai, *Sol. Energy Mater. Sol. Cells* **91**, 1202 (2007).
- ¹⁵⁸A. Morales-Acevedo, *Energy Procedia* **57**, 3051 (2014).
- ¹⁵⁹J. Li, D. R. Diercks, T. R. Ohno, C. W. Warren, M. C. Lonergan, J. D. Beach and C. A. Wolden, *Sol. Energy Mater. Sol. Cells* **133**, 208 (2015).
- ¹⁶⁰N. Strevel, L. Trippel, C. Kotarba and I. Khan, *Photovoltaics Int.* **22**, 66 (2014).
- ¹⁶¹J. D. Poplawsky, N. R. Paudel, C. Li, C. M. Parish, D. Leonard, Y. Yan and S. J. Pennycook, *Adv. Energy Mater.* **4**, 1400454 (2014).

- ¹⁶²C. Li, Y. Wu, J. Poplawsky, T. J. Pennycook, N. Paudel, W. Yin, S. J. Haigh, M. P. Oxley, A. R. Lupini, M. Al-Jassim, S. J. Pennycook, and Y. Yan, *Phys. Rev. Lett.* **112**, 156103 (2014).
- ¹⁶³I. Visoly-Fisher, S. R. Cohen, A. Ruzin and D. Cahen, *Adv. Mater.* **16**, 879 (2004).
- ¹⁶⁴I. Visoly-Fisher, S. R. Cohen, K. Gartsman, A. Ruzin and D. Cahen, *Adv. Funct. Mater.* **16**, 649 (2006).
- ¹⁶⁵J. R. Sites, J. E. Granata and J. F. Hiltner, *Sol. Energy Mater. Sol. Cells* **55**, 43 (1998).
- ¹⁶⁶P. Schulz, E. Edri, S. Kirmayer, G. Hodes, D. Cahen and A. Kahn, *Energy Environ. Sci.* **7**, 1377 (2014).
- ¹⁶⁷H.-S. Kim, C.-R. Lee, J.-H. Im, K.-B. Lee, T. Moehl, A. Marchioro, S.-J. Moon, R. Humphry-Baker, J.-H. Yum, J. E. Moser, M. Grätzel and N.-G. Park, *Sci. Rep.* **2**, 591 (2012).
- ¹⁶⁸L. Kavan and M. Grätzel, *Electrochim. Acta* **40**, 643 (1995).
- ¹⁶⁹R. Schölin, M. H. Karlsson, S. K. Eriksson, H. Siegbahn, E. M. J. Johansson and H. Rensmo, *J. Phys. Chem. C* **116**, 26300 (2012).
- ¹⁷⁰A. Guerrero, E. J. Juarez-Perez, J. Bisquert, I. Mora-Sero and G. Garcia-Belmonte, *Appl. Phys. Lett.* **105**, 133902 (2014).
- ¹⁷¹J. Shi, X. Xu, D. Li and Q. Meng, *Small* **21**, 2472 (2015).
- ¹⁷²C.-S. Jiang, M. Yang, Y. Zhou, B. To, S. U. Nanayakkara, J. M. Luther, W. Zhou, J. J. Berry, J. van de Lagemaat, N. P. Padture, K. Zhu and M. M. Al-Jassim, *Nat. Commun.* **6**, 8397 (2015).
- ¹⁷³V. W. Bergmann, S. A. L. Weber, F. J. Ramos, M. K. Nazeeruddin, M. Grätzel, D. Li, A. L. Domanski, I. Lieberwirth, S. Ahmad and R. Berger, *Nat. Commun.* **5**, 5001 (2014).
- ¹⁷⁴M. A. Green, A. Ho-Baillie and H. J. Snaith, *Nat. Photo.* **8**, 506 (2014).
- ¹⁷⁵W. Tress, N. Marinova, T. Moehl, S. M. Zakeeruddin, M. K. Nazeeruddin and M. Grätzel, *Energy Environ. Sci.* **8**, 995 (2015).
- ¹⁷⁶Y. Zhang, M. Liu, G. E. Eperon, T. C. Leijtens, D. McMeekin, M. Saliba, W. Zhang, M. de Bastiani, A. Petrozza, L. M. Herz, M. B. Johnston, H. Lin and H. J. Snaith, *Mater. Horiz.* **2**, 315 (2015).
- ¹⁷⁷C. Eames, J. M. Frost, P. R. F. Barnes, B. C. O'Regan, A. Walsh and M. S. Islam, *Nat. Commun.* **6**, 7497 (2015).
- ¹⁷⁸J. M. Ball, M. M. Lee, A. Hey and H. Snaith, *Energy Environ. Sci.* **6**, 1739 (2013).
- ¹⁷⁹C. C. Stoumpos, C. D. Malliakas and M. G. Kanatzidis, *Inorg. Chem.* **52**, 9019 (2013).

- ¹⁸⁰Q. Wang, Y. Shao, H. Xie, L. Lyu, X. Liu, Y. Gao and J. Huang, *Appl. Phys. Lett.* **105**, 163508 (2014).
- ¹⁸¹Q. Dong, Y. Fang, Y. Shao, P. Mulligan, J. Qiu, L. Cao and J. Huang, *Science* **347**, 967 (2015).
- ¹⁸²E. J. Juarez-Perez, M. Wußler, F. Fabregat-Santiago, K. Lakus-Wollny, E. Mankel, T. Mayer, W. Jaegermann and I. Mora-Sero, *J. Phys. Chem. Lett.* **5**, 680 (2014).
- ¹⁸³W.-J. Yin, T. Shi and Y. Yan, *Appl. Phys. Lett.* **104**, 063903 (2014).
- ¹⁸⁴W.-J. Yin, J.-H. Yang, J. Kang, Y. Yan and S.-H. Wei, *J. Mater. Chem. A* **3**, 8926 (2015).
- ¹⁸⁵J. Kim, S.-H. Lee, J. H. Lee and K.-H. Hong, *J. Phys. Chem. Lett.* **5**, 1312 (2014).
- ¹⁸⁶M. L. Agiorgousis, Y.-Y. Sun, H. Zeng and S. Zhang, *J. Am. Chem. Soc.* **136**, 14570 (2014).
- ¹⁸⁷Q. Chen, H. Zhou, T.-B. Song, S. Luo, Z. Hong, H.-S. Duan, L. Dou, Y. Liu and Y. Yang, *Nano Lett.* **14**, 4158 (2014).
- ¹⁸⁸J. S. Yun, A. Ho-Baillie, S. Huang, S. H. Woo, Y. Heo, J. Seidel, F. Huang, Y.-B. Cheng and M. A. Green, *J. Phys. Chem. Lett.* **6**, 875 (2015).
- ¹⁸⁹B. Yang, O. Dyck, J. Poplawsky, J. Keum, A. Puretzky, S. Das, I. Ivanov, C. Rouleau, G. Duscher, D. Geohegan and K. Xiao, *J. Am. Chem. Soc.* **137**, 9210 (2015).
- ¹⁹⁰H. D. Kim, H. Ohkita, H. Benten and S. Ito, *Adv. Mater.* **28**, 917 (2016).
- ¹⁹¹P. P. Altermatt, J. Schmidt, G. Heiser and A. G. Aberle, *J. Appl. Phys.* **82**, 4938 (1997).

Figures

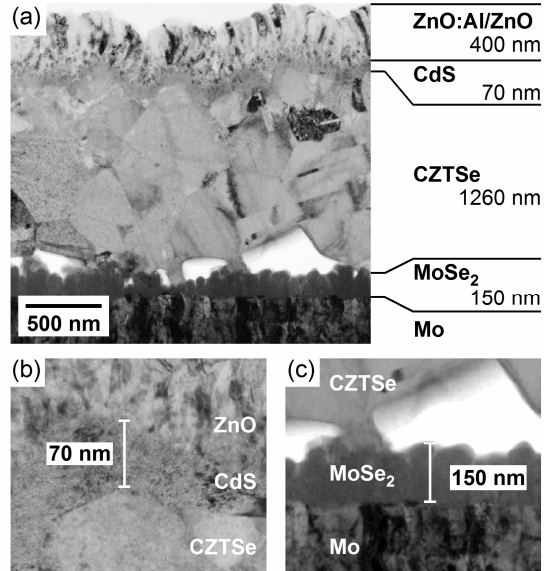


FIG. 1. Cross-sectional TEM images of the CZTSe solar cell fabricated in this study: (a) the whole solar-cell structure, (b) the enlarged image for the ZnO/CdS/CZTSe interface, and (c) the enlarged image for the CZTSe/Mo interface.

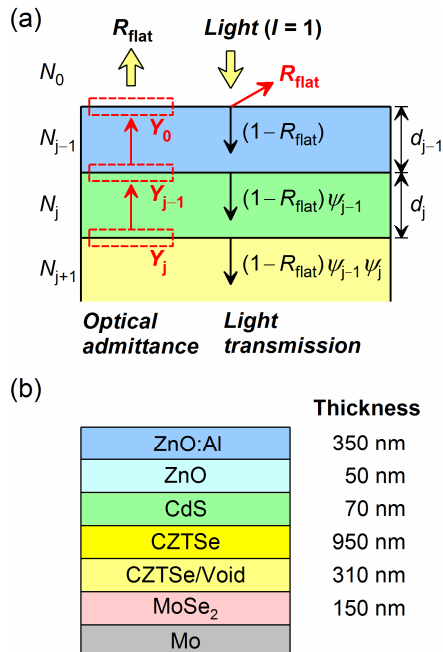


FIG. 2. (a) Calculation procedure of the optical admittance method and (b) optical model constructed for the CZTSe solar cell in Fig. 1.

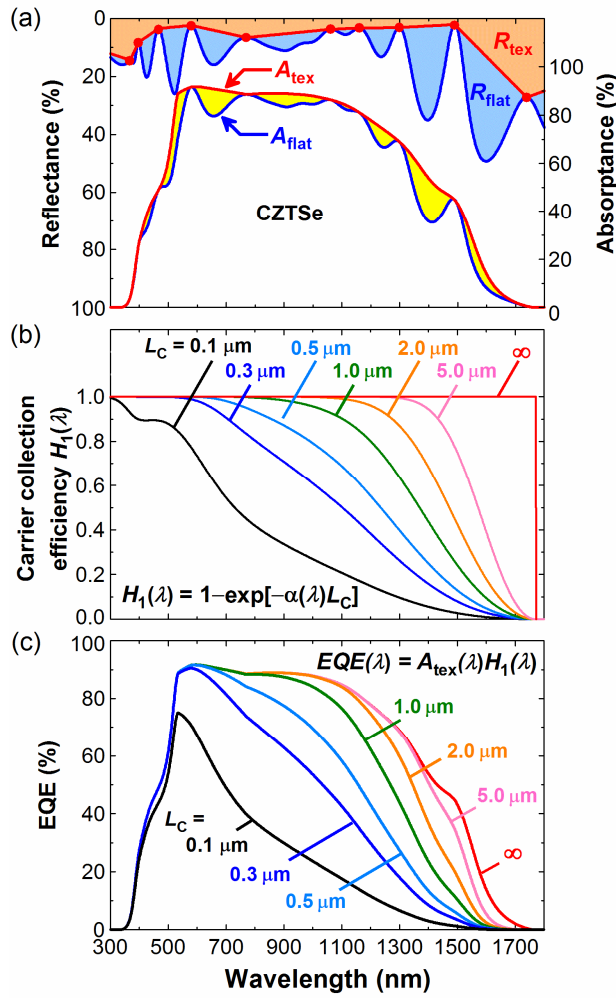


FIG. 3. Calculation procedure of the e-ARC method established in this study: (a) Reflectance spectra calculated assuming a flat structure (R_{flat}) and a textured structure (R_{tex}), together with the absorbance spectra of the CZTSe layer, A_{flat} and A_{tex} , obtained using R_{flat} and R_{tex} , respectively, (b) carrier collection efficiency $H_1(\lambda)$ calculated from the $\alpha(\lambda)$ of the CZTSe using different values of carrier collection length (L_c), and (c) EQE spectra of the CZTSe solar cell calculated based on the results of (a) and (b). This EQE simulation was performed using the optical model of Fig. 2(b).

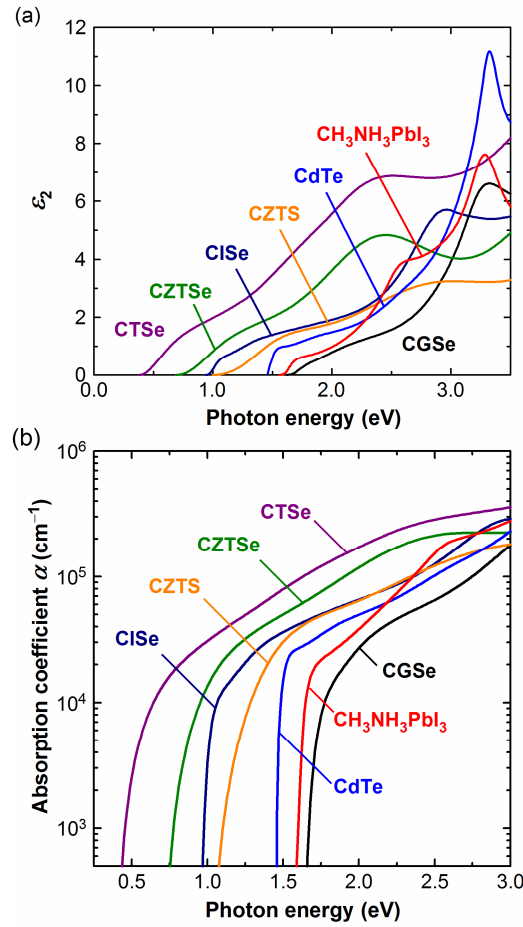


FIG. 4. (a) ϵ_2 spectra and (b) α spectra of various semiconductors applied for solar cells. In this figure, the reported optical data for CTSe,⁶¹ CZTSe,⁶¹ CISE,^{66,67} CZTS,⁶⁸ CGSe,^{66,67} CdTe,⁶⁹ and $\text{CH}_3\text{NH}_3\text{PbI}_3$ ⁶⁵ are shown.

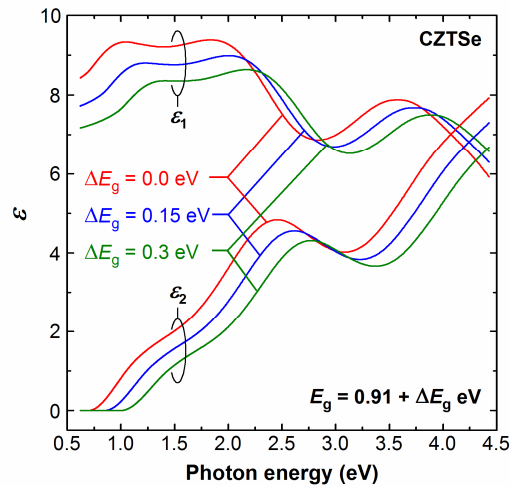


FIG. 5. Variation of the CZTSe dielectric function with the Cu content, calculated from Eq. (10) using different ΔE_g values. The dielectric function of $\Delta E_g = 0$ eV corresponds to that of the CZTSe in Fig. 4(a).

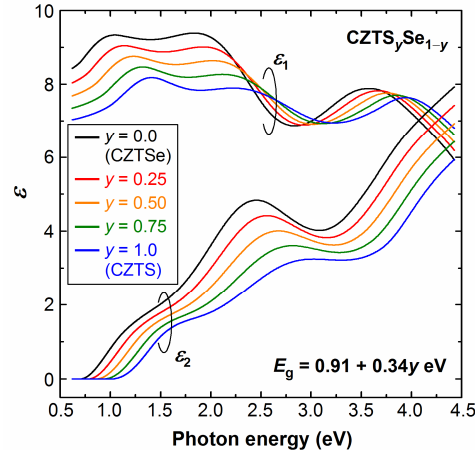


FIG. 6. Dielectric functions of $\text{CZTS}_y\text{Se}_{1-y}$ calculated by applying the energy shift model. The Cu content of the $\text{CZTS}_y\text{Se}_{1-y}$ is $x \sim 0.95$.

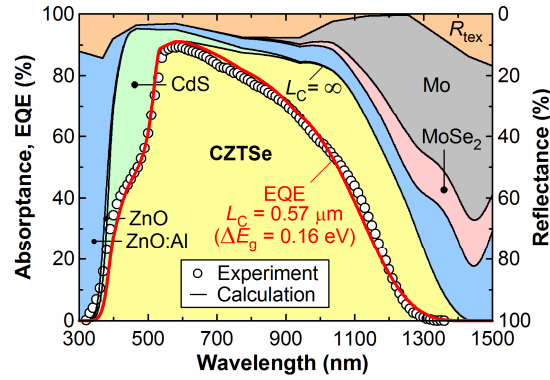


FIG. 7. Experimental EQE spectrum of the CZTSe solar cell consisting of ZnO:Al (350 nm)/ZnO (50 nm)/CdS (70 nm)/CZTSe (950 nm)/CZTSe-void (310 nm)/MoSe₂ (150 nm)/Mo (open circles), together with the fitted EQE result (red line) obtained from the e-ARC method assuming $L_C = 0.57 \mu\text{m}$ and $\Delta E_g = 0.16$ eV. The absorbance spectra of the solar-cell component layers and R_{tex} determined from the ARC method are shown by the black lines.

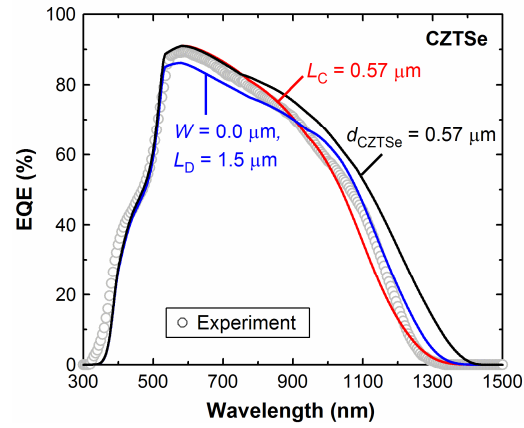


FIG. 8. Results of the EQE fitting analyses for the CZTSe solar cell using different $H(\lambda)$ functions and optical models. The red and blue lines represent the results of the EQE fitting analyses using $H_1(\lambda)$ [Eq. (5)] and $H_2(\lambda)$ [Eq. (7)], respectively, while the black line indicates the result when the total thickness of the CZTSe layer (d_{CZTSe}) is assumed to be $0.57 \mu\text{m}$. The experimental data (gray open circles) and the calculation result (red line) correspond to those of Fig. 7.

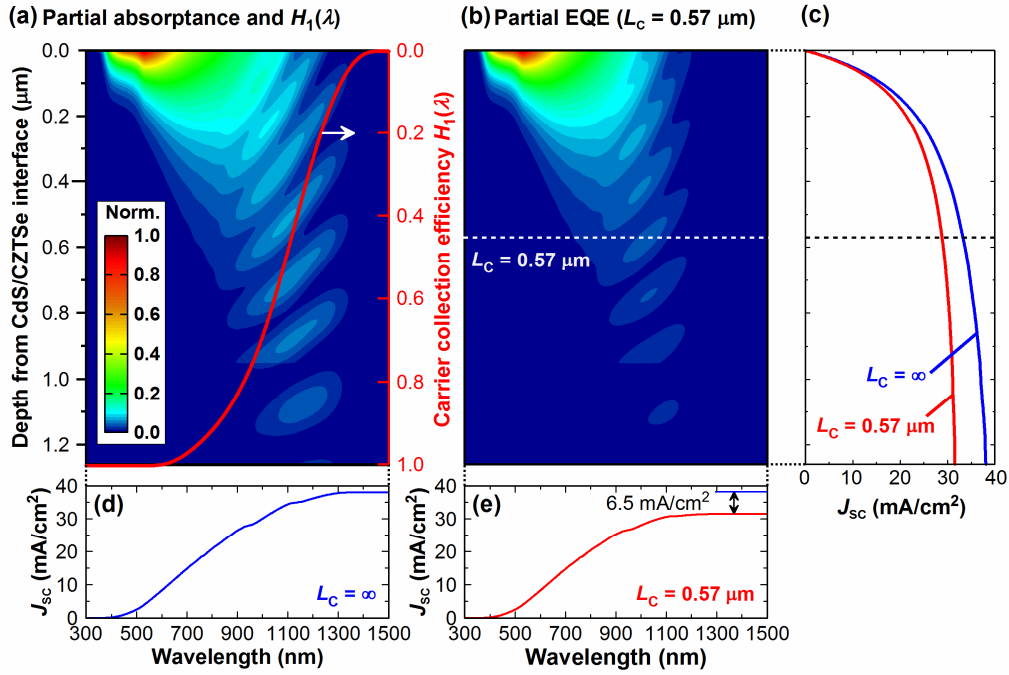


FIG. 9. (a) Partial A of the CZTSe layer in the solar cell obtained at different depths from the CdS/CZTSe interface and wavelengths, together with $H_1(\lambda)$ obtained assuming $L_C = 0.57 \mu\text{m}$, (b) partial EQE of the CZTSe calculated assuming $L_C = 0.57 \mu\text{m}$, (c) integrated J_{sc} for d , (d) integrated J_{sc} for λ when $L_C = \infty$ and (e) integrated J_{sc} for λ when $L_C = 0.57 \mu\text{m}$. In (a) and (b), the calculated values are normalized by the maximum values and the result of $d > 0.95 \mu\text{m}$ corresponds to the CZTSe/void region in Fig. 2(b).

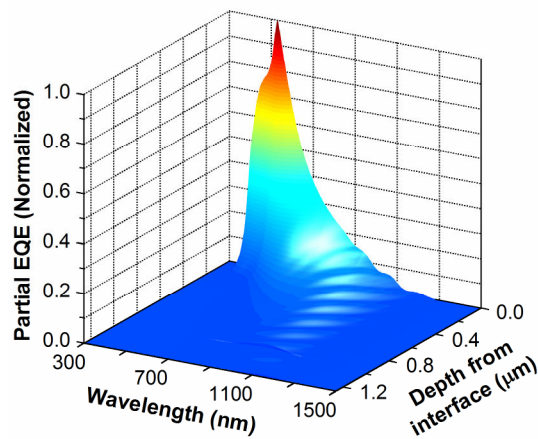


FIG. 10. Normalized partial EQE of the CZTSe solar cell. The partial EQE values correspond to those shown in Fig. 9(b).

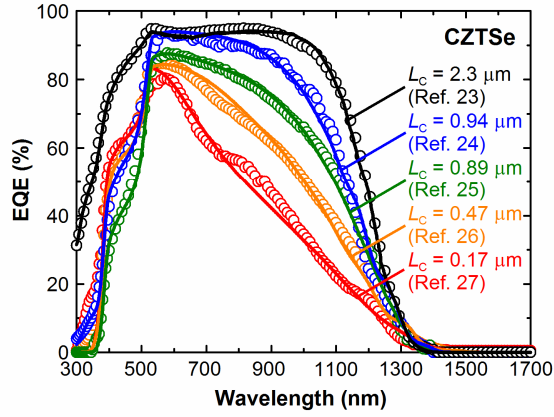


FIG. 11. Experimental EQE spectra of various CZTSe solar cells reported in Refs. 23-27 (open circles) and the results of the EQE fitting analyses performed for these solar cells using the e-ARC method (solid lines). The L_C values obtained from the EQE analyses are also shown.

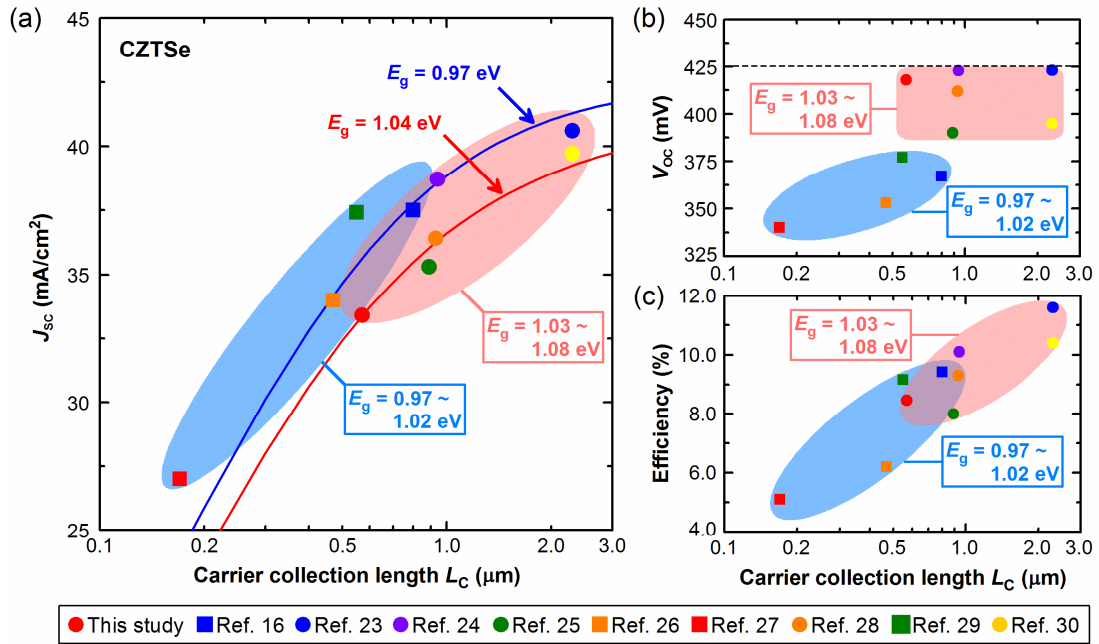


FIG. 12. (a) J_{sc} , (b) V_{oc} and (c) efficiency of reported CZTSe solar cells (Refs. 16, 23-30) as a function of L_C deduced from the EQE analyses using the e-ARC method. Based on the E_g values obtained from the EQE analyses, the CZTSe active layers are categorized into two groups of $E_g = 0.97\text{--}1.02$ eV (closed squares) and $E_g = 1.03\text{--}1.08$ eV (closed circles). The solid lines show the variations of J_{sc} with L_C , calculated assuming $E_g = 0.97$ eV (blue line) and 1.04 eV (red line). For these simulations, a uniform CZTSe layer ($2.0\ \mu\text{m}$ thickness) without the void component is assumed in the optical model of Fig. 2(b).

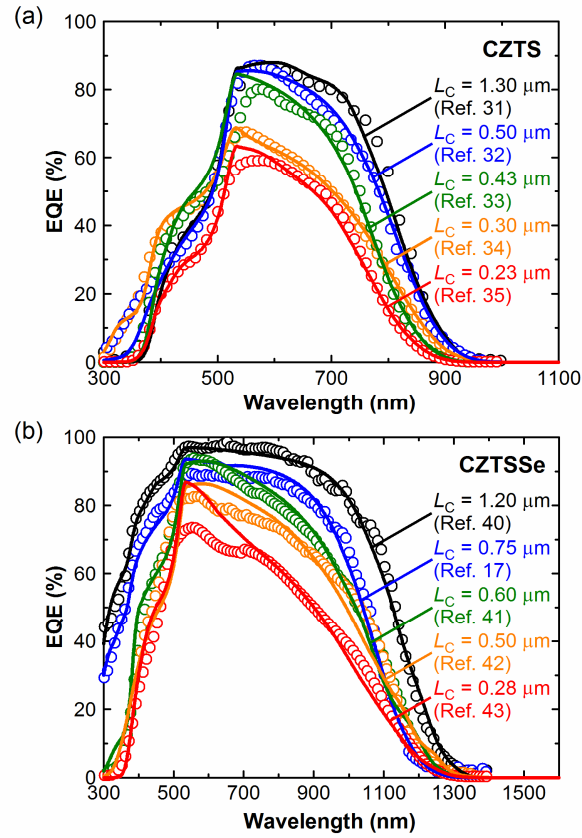


FIG. 13. Experimental EQE spectra of (a) CZTS solar cells reported in Refs. 31-35 and (b) CZTSSe solar cells reported in Refs. 17, 40-43 (open circles), together with the results of the EQE fitting analyses performed for these solar cells using the e-ARC method (solid lines). The L_C values obtained from the EQE analyses are also shown.

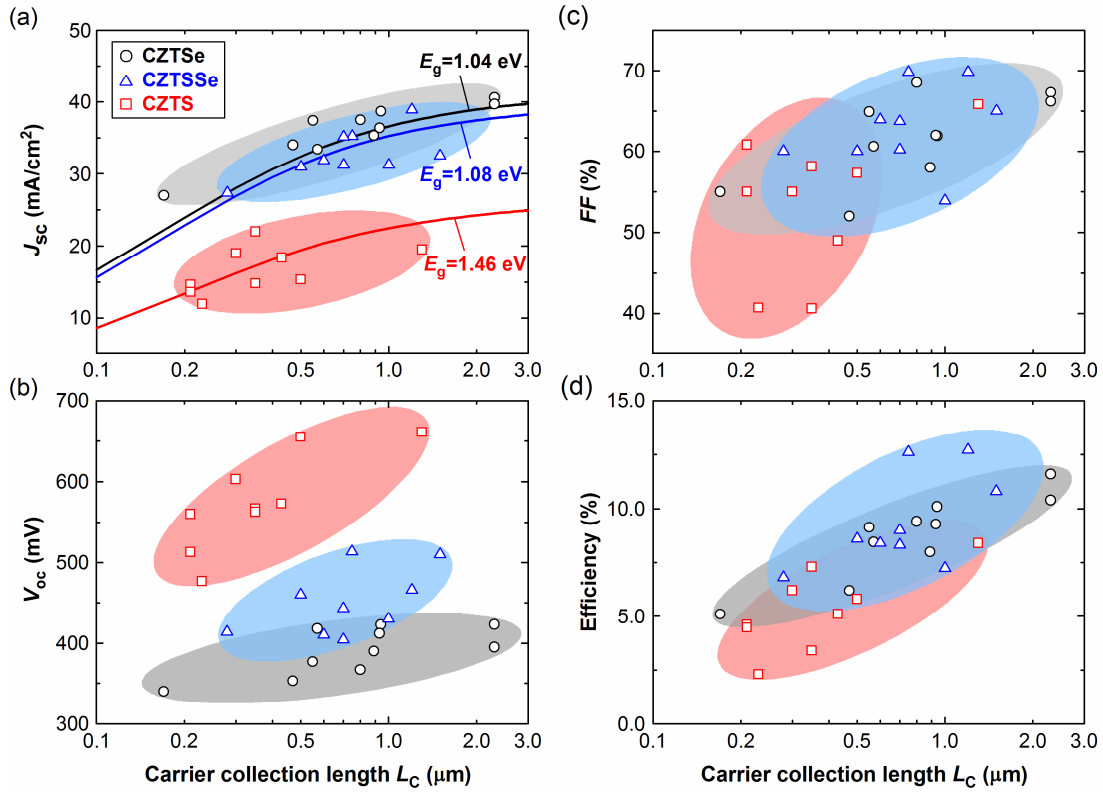


FIG. 14. (a) J_{sc} , (b) V_{oc} , (c) FF and (d) efficiency of reported CZTSe (Refs. 16, 23-30), CZTS (Refs. 31-39) and CZTSSe (Refs. 17, 40-47) solar cells as a function of L_C deduced from the EQE analyses using the e-ARC method. The solid lines indicate the variations of J_{sc} with L_C , calculated assuming the E_g values of 1.04 eV (CZTSe), 1.08 eV (CZTSSe) and 1.46 eV (CZTS).

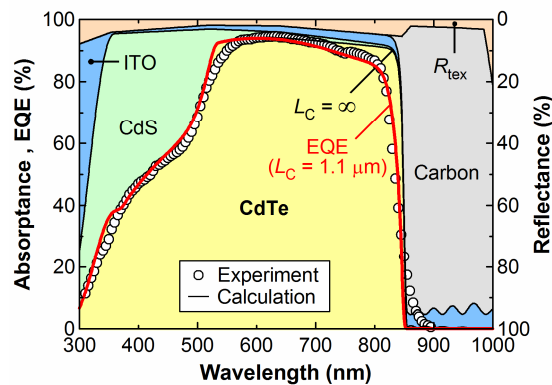


FIG. 15. Experimental EQE spectrum of a CdTe solar cell consisting of MgF_2 /glass/ITO (200 nm)/CdS (50 nm)/CdTe (3.5 μm)/carbon electrode,⁴⁸ together with the fitted EQE result (red line) obtained from the e-ARC method assuming $L_C = 1.1 \mu m$. The A spectra of the solar-cell component layers and R_{tex} determined from the ARC method are also shown by the black lines.

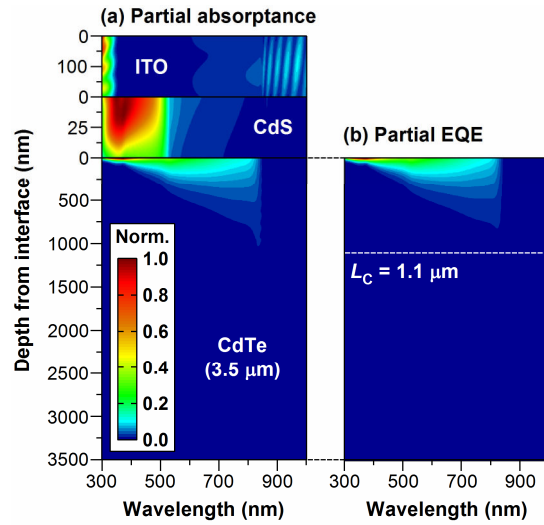


FIG. 16. (a) Partial A for the ITO (200 nm)/CdS (50 nm)/CdTe ($3.5 \mu\text{m}$) and (b) partial EQE of the CdTe layer ($L_C = 1.1 \mu\text{m}$) for the CdTe device in Fig. 15. The partial A and EQE values are normalized by the maximum values in each layer.

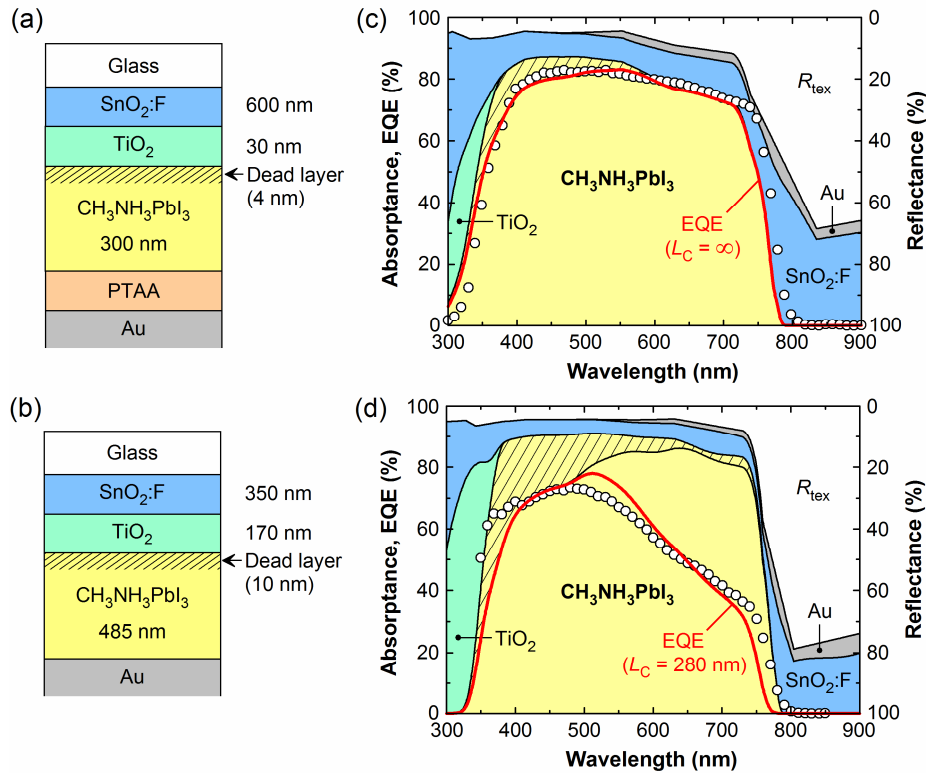


FIG. 17. Optical models for $\text{CH}_3\text{NH}_3\text{PbI}_3$ solar cells (a) with an HTL (Ref. 49) and (b) with no HTL (Ref. 50), and the corresponding EQE analysis results for the $\text{CH}_3\text{NH}_3\text{PbI}_3$ solar cells (c) with the HTL and (d) with no HTL. In (a) and (b), the values represent the layer thicknesses in the optical model, and the thickness of the PTAA layer in (a) is assumed to be zero. For the $\text{CH}_3\text{NH}_3\text{PbI}_3$ layers, the presence of optical dead layers near the TiO_2 interface is assumed.

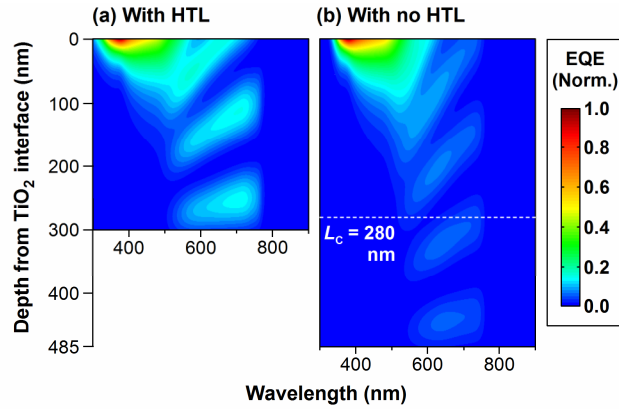


FIG. 18. Partial EQE obtained at different depths from the $\text{TiO}_2/\text{CH}_3\text{NH}_3\text{PbI}_3$ interface in the $\text{CH}_3\text{NH}_3\text{PbI}_3$ solar cells (a) with the HTL and (b) with no HTL. These partial EQE values correspond to the EQE spectra shown as the red lines in Fig. 17. The partial EQE values are normalized by the maximum values in each solar cell. In (b), the dotted line indicates the position of $L_C = 280$ nm.

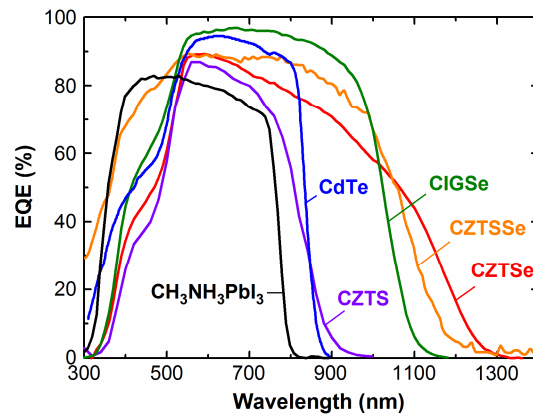


FIG. 19. Experimental EQE spectra for various solar cells: CZTSe (Fig. 7), CZTSSe [Ref. 17 in Fig. 13(b)], CIGSe (Ref. 19), CZTS [Ref. 31 in Fig. 13(a)], CdTe (Ref. 48 in Fig. 15) and $\text{CH}_3\text{NH}_3\text{PbI}_3$ [Ref. 49 in Fig. 17(c)].

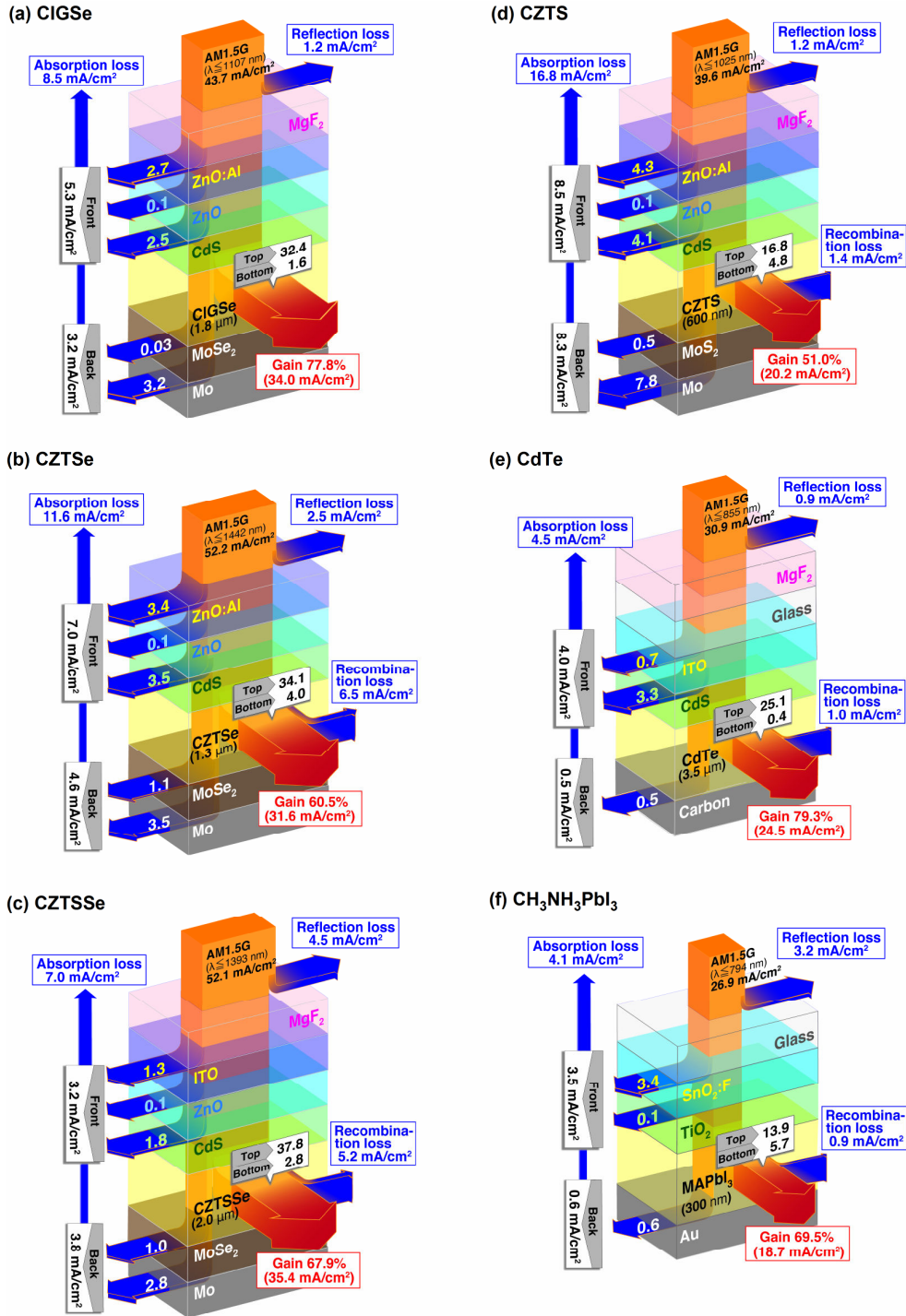


FIG. 20. Optical and recombination losses deduced from the EQE analyses performed for the spectra of Fig. 19: (a) CIGSe, (b) CZTSe, (c) CZTSSe, (d) CZTS, (e) CdTe, and (f) CH₃NH₃PbI₃ (MAPbI₃). The numerical values represent the corresponding current densities in units of mA/cm². The maximum J_{sc} value attainable under AM1.5G condition and the J_{sc} contributions obtained assuming two sublayers (top and bottom layers) with an equal thickness are also indicated. The optical gain represents the ratio of output J_{sc} divided by the maximum-attainable J_{sc} value. The result of the CIGSe is adopted from Ref. 19.

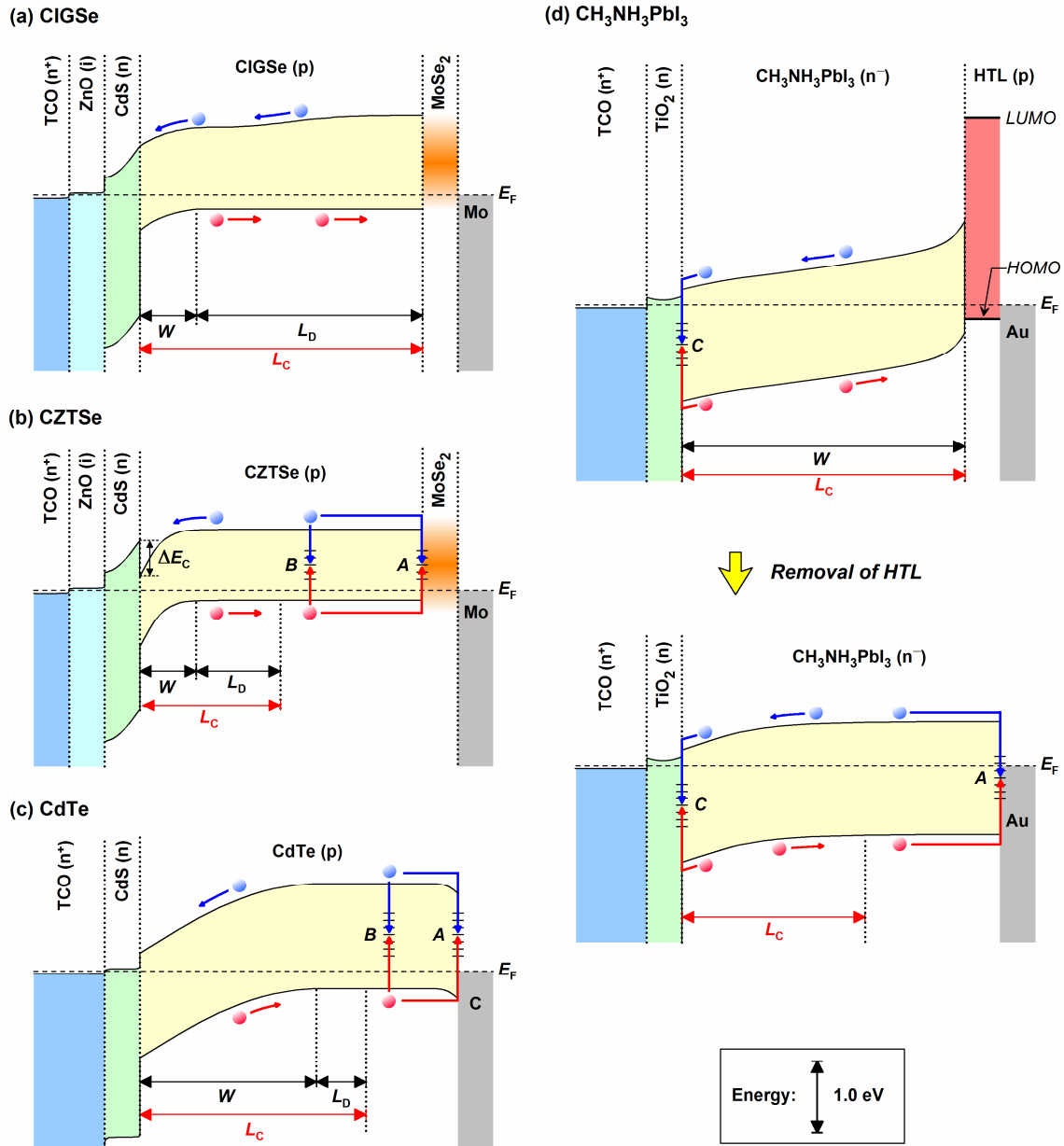


FIG. 21. Band diagrams for various solar cells of (a) CIGSe, (b) CZTSe, (c) CdTe, and (d) $\text{CH}_3\text{NH}_3\text{PbI}_3$ with an HTL (spiro-OMeTAD) and with no HTL. In this figure, *A*, *B* and *C* represent the recombination processes in the rear interface, bulk and front interface regions, respectively.

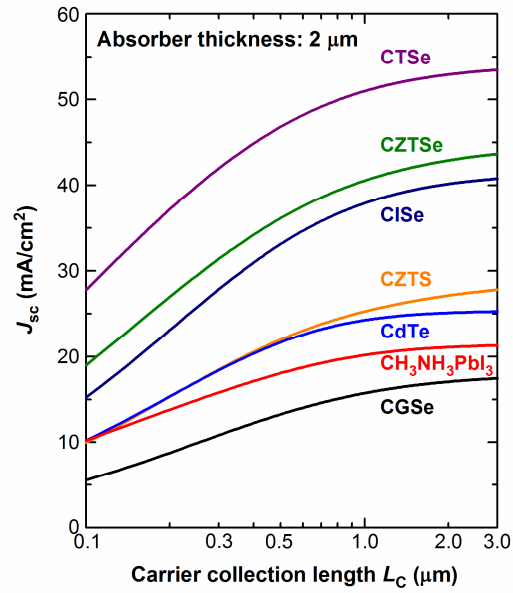


FIG. 22. Variation of J_{sc} with L_c for various solar cells calculated from the e-ARC method. For all the solar cells, an identical solar cell structure consisting of the MgF_2 (130 nm)/ ZnO:Al (360 nm)/ ZnO (50 nm)/ CdS (45 nm)/absorber ($2.0 \mu\text{m}$)/ Mo is assumed, except for CdTe and $\text{CH}_3\text{NH}_3\text{PbI}_3$ solar cells. For the CdTe and $\text{CH}_3\text{NH}_3\text{PbI}_3$ solar cells, the structures in Fig. 15 (CdTe) and Fig. 17(a) ($\text{CH}_3\text{NH}_3\text{PbI}_3$) were adopted, but the CdTe and $\text{CH}_3\text{NH}_3\text{PbI}_3$ thicknesses were assumed to be $2.0 \mu\text{m}$.